The Astrophysical Journal, 1007:38 (27pp), 2026 August 10 https://doi.org/10.3847/1538-4357/ae83b2

Multiwavelength Analysis of Six Luminous Fast Blue Optical Transients

Cassie Sevilla[1,34], Anna Y. Q. Ho[1], Nayana A.J.[2,3], Steve Schulze[4], Daniel A. Perley[5], Michael Bremer[6], Igor Andreoni[7], Ivan Altunin[8], Thomas G. Brink[2], Michael Camilo[1], Poonam Chandra[9], Ping Chen[10,11,12], Ashley A. Chrimes[13,14], Michael W. Coughlin[15], Kaustav K. Das[16], Andrew Drake[16], Alexei V. Filippenko[2], Christoffer Fremling[17,18], James Freeburn[19,20,7], Avishay Gal Yam[12], Mary Gerhart[2], Matthew J. Graham[18], George Helou[18], K-Ryan Hinds[5], Natalya Johnson[21], Mansi M. Kasliwal[18], Harsh Kumar[22,23], Russ R. Laher[24], Natalie LeBaron[2,3], Maggie L. Li[16], Chang Liu[25,4,26], Ben Margalit[15], Yu-Jing Qin[16], Nabeel Rehemtulla[25,4,26], Sophia Risin[2], Sam Rose[18], Rupak Roy[27], Ben Rusholme[24], Genevieve Schroeder[1], Jesper Sollerman[28], Gokul P. Srinivasaragavan[29,30,31,18], Kailai Wang[1], Jacob L. Wise[5], Yi Yang[2,32], Yuhan Yao[33,2], and WeiKang Zheng[2]

[1] Department of Astronomy, Cornell University, Ithaca, NY 14853, USA
[2] Department of Astronomy, University of California, Berkeley, CA 94720-3411, USA
[3] Berkeley Center for Multi-messenger Research on Astrophysical Transients and Outreach (Multi-RAPTOR), University of California, Berkeley, CA 94720-3411, USA
[4] Center for Interdisciplinary Exploration and Research in Astrophysics (CIERA), Northwestern University, 1800 Sherman Avenue, Evanston, IL 60201, USA
[5] Astrophysics Research Institute, Liverpool John Moores University, IC 2, Liverpool Science Park, 146 Brownlow Hill, Liverpool L3 5RF, UK
[6] Institut de Radio Astronomie Millimétrique (IRAM), 300 rue de la Piscine, 38406, Saint Martin d'Hères, France
[7] Department of Physics and Astronomy, University of North Carolina at Chapel Hill, Chapel Hill, NC 27599-3255, USA
[8] Department of Physics, University of Nevada, Reno, NV 89557, USA
[9] National Radio Astronomy Observatory, 520 Edgemont Road, Charlottesville, VA 22903-2475, USA
[10] Institute for Advanced Study in Physics, Zhejiang University, Hangzhou 310027, People's Republic of China
[11] Institute for Astronomy, School of Physics, Zhejiang University, Hangzhou 310027, People's Republic of China
[12] Department of Particle Physics and Astrophysics, Weizmann Institute of Science, 234 Herzl Street, 7610001 Rehovot, Israel
[13] European Space Agency (ESA), European Space Research and Technology Centre (ESTEC), Keplerlaan 1, 2201 AZ Noordwijk, The Netherlands
[14] Department of Astrophysics/IMAPP, Radboud University, PO Box 9010, 6500 GL Nijmegen, The Netherlands
[15] School of Physics and Astronomy, University of Minnesota, Minneapolis, MN 55455, USA
[16] Cahill Center for Astrophysics, California Institute of Technology, MC 249-17, 1200 East California Boulevard, Pasadena, CA 91125, USA
[17] Caltech Optical Observatories, California Institute of Technology, Pasadena, CA 91125, USA
[18] Division of Physics, Mathematics and Astronomy, California Institute of Technology, Pasadena, CA 91125, USA
[19] Centre for Astrophysics and Supercomputing, Swinburne University of Technology, VIC 3122, Australia
[20] ARC Centre of Excellence for Gravitational Wave Discovery (OzGrav), VIC 3122, Australia
[21] Department of Physics, Drexel University, Philadelphia, PA 19104, USA
[22] Center for Astrophysics | Harvard & Smithsonian, 60 Garden Street, Cambridge, MA 02138-1516, USA
[23] The NSF AI Institute for Artificial Intelligence and Fundamental Interactions, USA
[24] IPAC, California Institute of Technology, 1200 East California Boulevard, Pasadena, CA 91125, USA
[25] Department of Physics and Astronomy, Northwestern University, 2145 Sheridan Road, Evanston, IL 60208, USA
[26] NSF-Simons AI Institute for the Sky (SkAI), 172 East Chestnut Street, Chicago, IL 60611, USA
[27] Institute of Astronomy Space and Earth Science (IASES), P 177, CIT Road, Scheme 7m, Kolkata 700054, West Bengal, India
[28] The Oskar Klein Centre, Department of Astronomy, AlbaNova, Stockholm University, SE-106 91 Stockholm, Sweden
[29] Department of Astronomy, University of Maryland, College Park, MD 20742, USA
[30] Joint Space-Science Institute, University of Maryland, College Park, MD 20742, USA
[31] Astrophysics Science Division, NASA Goddard Space Flight Center, 8800 Greenbelt Road, Greenbelt, MD 20771, USA
[32] Department of Physics, Tsinghua University, Qinghua Yuan, Beijing 100084, People's Republic of China
[33] Miller Institute for Basic Research in Science, 206B Stanley Hall, Berkeley, CA 94720, USA
Received 2026 January 27; revised 2026 June 22; accepted 2026 June 22; published 2026 August 4

Abstract

We present early ($\lesssim$1 yr) multiwavelength observations and analysis of six luminous fast blue optical transients (LFBOTs). We identified these LFBOTs in Zwicky Transient Facility survey data from their fast light-curve evolution ($t_{1/2} \leqslant 12$ days), blue colors at peak brightness ($g - r \leqslant -0.2$ mag), a visible host galaxy, high optical luminosity ($M_g < -20$ mag), and an X-ray and/or radio detection. With the exception of AT2024aehp (ZTF24abygbss), these transients exhibit peaks in their 10 GHz radio light curves at $t_{\rm rest} \approx 50$–100 days, with peak radio luminosities ranging from 10^{38} to 10^{40} erg s^{-1}. Modeling the radio emission as synchrotron radiation indicates a fast ($v = 0.1$–$0.3c$) shock in a dense ($n_e \approx 10^3$–10^4 cm^{-3}) medium. The X-ray emission varies by $\approx$2 orders of magnitude in luminosity (10^{42}–10^{44} erg s^{-1}) at $t_{\rm rest} \sim 20$ days. Analysis of the host-galaxy photometry and spectroscopy for each transient shows that LFBOTs are predominantly nonnuclear (a few kiloparsecs offset) with star-forming host galaxies of stellar masses $= 10^9$–10^{11} $M_\odot$. Unlike all other LFBOTs to date, AT2024aehp exhibited a luminous ($M < -19$ mag) plateau in the optical light curve and its 6–15 GHz radio emission brightened by over an order of magnitude from $t_{\rm rest} \approx 70$ to

[34] Corresponding author.

130 days. The mostly consistent radio behavior between these LFBOTs implies a similar circumburst medium, leading us to prefer a progenitor scenario in which mass is lost in a consistent way shortly prior to the terminal event.

Unified Astronomy Thesaurus concepts: Transient detection (1957); Transient sources (1851); High energy astrophysics (739); Radio transient sources (2008); X-ray transient sources (1852); Time domain astronomy (2109); Observational astronomy (1145); Optical astronomy (1776); Time series analysis (1916)

Materials only available in the online version of record: machine-readable tables

1. Introduction

The advent of high-cadence optical surveys such as the Asteroid Terrestrial-impact Last Alert System (ATLAS; J. L. Tonry et al. 2018) and the Zwicky Transient Facility (ZTF; E. C. Bellm et al. 2019; M. J. Graham et al. 2019; R. Dekany et al. 2020) has led to the discovery of new classes of extragalactic transients. Some of these transients are referred to as fast blue optical transients (FBOTs), most famously AT2018cow (e.g., S. J. Prentice et al. 2018). FBOTs are typically defined as transients with blue colors ($g - r \leqslant -0.2$ mag), rapid time evolution (<12 days above half-maximum brightness), and extragalactic nature (M. R. Drout et al. 2014; M. Pursiainen et al. 2018; C. Inserra 2019).

In this paper, we focus on a particular subset of FBOTs dubbed "AT2018cow-like" transients (A. Y. Q. Ho et al. 2023b) or luminous FBOTs (LFBOTs; B. D. Metzger 2022; J. Klencki & B. D. Metzger 2026). The term LFBOT is empirical and has been used to describe optically discovered transients with very similar optical, radio, and X-ray light curves to AT2018cow (e.g., D. L. Coppejans et al. 2020; D. A. Perley et al. 2021, 2026; J. S. Bright et al. 2022; A. Y. Q. Ho et al. 2022b; C. P. Gutiérrez et al. 2024; A. J. Nayana et al. 2025; N. LeBaron et al. 2026) as well as blue optical counterparts to gamma-ray bursts (GRBs; e.g., D. L. A. Pieterse et al. 2026). In this paper, we use the term LFBOT to refer to an FBOT with high optical brightness ($M_g < -20$ mag) and luminous X-ray and/or radio emission.

There are currently eight published transients discovered by optical surveys that fall under this empirical classification (Table 1). It is theorized that the peak of their optical light curves results from shock breakout from a dense medium (E. O. Ofek et al. 2010; M. Pursiainen et al. 2018) or from a jet cocoon (O. Gottlieb et al. 2022). The radio emission is found to be consistent with synchrotron radiation emanating from a fast to mildly relativistic shock (R. Margutti et al. 2019; D. L. Coppejans et al. 2020; A. Y. Q. Ho et al. 2020a). The X-ray radiation is suggested to come from a central X-ray source, separate from the synchrotron radiation that powers the radio (A. Y. Q. Ho et al. 2019; R. Margutti et al. 2019). For objects with high-cadence X-ray observations (AT2018cow, AT2020mrf, AT2022tsd, and AT2024wpp) it was found that the X-rays had fast variability on a timescale of minutes to days (L. E. Rivera Sandoval et al. 2018; R. Margutti et al. 2019; Y. Yao et al. 2022; A. Y. Q. Ho et al. 2023c; A. J. Nayana et al. 2025; D. A. Perley et al. 2026).

Based on the first few LFBOTs discovered, B. D. Metzger (2022) argued that progenitor models must reconcile two key characteristics: a dense surrounding medium and a long-lived central engine. Some propositions include tidal disruption events (TDEs) involving an intermediate-mass black hole (N. P. M. Kuin et al. 2019; D. A. Perley et al. 2019; C. P. Gutiérrez et al. 2024), the direct collapse (failed explosion) of a supergiant star (R. Margutti et al. 2019; D. A. Perley et al. 2019; A. A. Chrimes et al. 2026), and the tidal disruption of a star by a stellar-mass black hole resulting from a merger (B. D. Metzger 2022; J. Klencki & B. D. Metzger 2026) or random interactions in a cluster (K. Kremer et al. 2021, 2023).

Our understanding of LFBOTs has been limited in part by the small sample size, particularly the number that have multiwavelength data. Some behavior has only been observed in a single object, such as luminous UV emission years after AT2018cow (A. Inkenhaag et al. 2025), late-time luminous X-ray emission in AT2020mrf (Y. Yao et al. 2022), and minutes-duration optical flares in AT2022tsd (A. Y. Q. Ho et al. 2023c)—and it is not clear how prevalent this behavior is among LFBOTs. The rarity of these transients and the recency of the development of optical surveys like ZTF has limited the discovery rate.

Here we present early ($\lesssim$1 yr) multiwavelength observations of five new LFBOTs, as well as further radio observations on a sixth (AT2023fhn), increasing the sample size by over 50%. Section 2 describes the observations and data reduction. In Section 3 we model the radio emission as self-absorbed synchrotron radiation. In Section 4 we analyze the offsets from each LFBOT to its host galaxy, and each host galaxy's properties. Throughout, we use methods that are similar to those employed in previous LFBOT papers in order to make effective comparisons. We present our discussion and conclusions in Section 5, including suggestions for future LFBOT studies.

Throughout this paper, we assume a flat ΛCDM cosmology with $H_0 = 67.4\,\mathrm{km\,s^{-1}\,Mpc^{-1}}$ and $\Omega_M = 0.315$ (Planck Collaboration et al. 2020). All usages of $t_{\rm obs}$ refer to the time after the optical light-curve peak in the observer frame, while $t_{\rm rest}$ refers to this time in the rest frame. All dates are in UTC and all magnitudes are in AB.

2. Observations

The basic characteristics for all LFBOTs are listed in Table 1. The discovery details for AT2022abfc, AT2023fhn, AT2023hkw, AT2023vth, AT2024qfm, and AT2024aehp are given in Appendix A. Here we provide details on our multiwavelength follow-up observations.

2.1. Optical Photometry

After each LFBOT was identified in ZTF photometry (outlined in Appendix A), we obtained follow-up optical photometry using the Liverpool Telescope (LT; I. A. Steele et al. 2004) and the Spectral Energy Distribution (SED) Machine (SEDM; N. Blagorodnova et al. 2018; M. Rigault et al. 2019; Y.-L. Kim et al. 2022) on the Palomar 60 inch (1.5 m) telescope (P60; S. B. Cenko et al. 2006). For AT2024aehp, we also have UV data from the Neil Gehrels Swift Observatory (Swift; N. Gehrels et al. 2004) Ultra-Violet/Optical Telescope (P. W. A. Roming et al. 2005). For AT2024qfm, we also present photometry from the Alhambra Faint Object Spectrograph and Camera (ALFOSC) on the 2.56 m Nordic Optical Telescope (NOT; A. A. Djupvik & J. Andersen 2010), the Inamori-Magellan Areal Camera & Spectrograph (IMACS; A. Dressler 2011) mounted on the 6.5 m Magellan-Baade telescope, the Large Monolithic Imager (LMI)

Table 1
Luminous Fast Blue Optical Transient Summary

TNS Name	Survey Name	Redshift	R.A. (J2000) (HH:MM:SS.SSS)	Decl. (J2000) (DD:MM:SS.SS)	Offset (kpc)	t_0 (UTC)	References
AT2022abfc	ZTF22abvrxkk	0.212	4:51:19.200	−26:58:41.59	2.0	2022-11-21 08:15:48	This work
AT2023fhn	ZTF23aaeozpp/ATLAS23hnk	0.24	10:08:03.805	21:04:26.70	17	2023-04-12 05:22:39	[1, 2]; this work
AT2023hkw	ZTF23aaimsja	0.339	10:42:17.748	52:29:19.03	15	2023-04-30 04:08:52	This work
AT2023vth	ZTF23ableqsp	0.0747	17:56:34.403	8:02:37.30	3	2023-10-20 03:08:39	This work
AT2024qfm	ZTF24aaxhxhf/PS24hhm	0.2270	23:21:23.450	+11:56:31.99	3.7	2024-07-27 08:18:46	This work; [14]
AT2024aehp	ZTF24abygbss	0.1715	8:21:07.474	28:44:22.17	0.47	2024-12-19 10:02:49	This work
…	CSS161010	0.033	04:58:34.396	−08:18:03.95	0.28	2016-10-10 11:31:12	[3, 4]
AT2018lug	ZTF18abvkwla	0.2714	02:00:15.194	+16:47:57.32	1.9	2018-09-12 09:46:48	[5]
AT2018cow	ATLAS18qqn/ZTF18abcfcoo/Gaia18bqa	0.014145	16:16:00.220	+22:16:04.91	1.7	2018-06-16 10:35:02	[6]
AT2020mrf	ZTF20abfhyil/ATLAS20paa	0.1353	15:47:54.163	+44:39:07.41	1.19	2020-06-15 08:55:40	[7]
AT2020xnd	ZTF20acigmel	0.2433	22:20:02.030	−02:50:25.30	0.8	2020-10-12 04:06:03	[8]
AT2022tsd	ZTF22abftjko/PS22jvi	0.2564	03:20:10.863	+08:44:55.63	6	2022-09-07 11:21:22	[9]
AT2024wpp	GOTO24gjk/ZTF24abjjpbo/ PS24jhj/ATLAS24ond	0.0868	02:42:05.499	−16:57:22.90	5	2024-09-26 01:24:35	[10–13]

Note. Basic information on each LFBOT, such as position and redshift. The six LFBOTs discussed in this paper are presented first, while the rest of the known LFBOT population are shown below. t_0 is chosen to be the peak of the optical light curve. The redshift errors are to the last reported digit. Positions of the six LFBOTs presented in the paper and AT2020xnd were determined using the methodology in Section 4.1.

References. [1] A. A. Chrimes et al. (2024a), [2] A. A. Chrimes et al. (2024b), [3] D. L. Coppejans et al. (2020), [4] C. P. Gutiérrez et al. (2024), [5] A. Y. Q. Ho et al. (2020a), [6] S. J. Prentice et al. (2018), [7] Y. Yao et al. (2022), [8] D. A. Perley et al. (2021), [9] A. Y. Q. Ho et al. (2023c), [10] M. Pursiainen et al. (2025), [11] A. J. Nayana et al. (2025), [12] N. LeBaron et al. (2026), [13] D. A. Perley et al. (2026), and [14] A. J. Nayana et al. (2026, in preparation).

on the 4.3 m Lowell Discovery Telescope (LDT; T. A. Bida et al. 2014), and the Goodman High Throughput Spectrograph (GHTS; J. C. Clemens et al. 2004) camera on the 4.1 m Southern Astrophysical Research (SOAR) Telescope.[35] We correct for Milky Way extinction using the `extinction` Python package,[36] using the prescription of E. F. Schlafly & D. P. Finkbeiner (2011) and $R_V = 3.1$.

The optical light curves of each object are shown in Figure 1. For each object, $t_{\rm rest} = t_{\rm obs} = 0$ was chosen to match the peak of the transient's optical light curve. To convert to absolute magnitude, we apply the conversion

$$M = m_{\rm obs} - 5\log_{10}\left(\frac{D_L}{10\ {\rm pc}}\right) + 2.5\log_{10}(1+z). \quad (1)$$

2.2. Optical Spectroscopy

As part of our follow-up campaigns, we collected optical spectra at $t_{\rm obs} = 4$–37 days. We utilized the following facilities: the Gemini Multi-Object Spectrograph (GMOS; I. M. Hook et al. 2004; G. Gimeno et al. 2016), the Keck Low-Resolution Imaging Spectrometer (LRIS; J. B. Oke et al. 1995) on the 10 m Keck I telescope, the Keck Cosmic Web Imager (KCWI; P. Morrissey et al. 2018) and the Deep Imaging Multi-Object Spectrograph (DEIMOS; S. M. Faber et al. 2003) on the 10 m Keck II telescope, the Double Spectrograph (DBSP) on the Palomar 5 m telescope (J. B. Oke & J. E. Gunn 1982), and the Binospec instrument (D. Fabricant et al. 2019) on the 6.5 m MMT. The basic details for each spectroscopic observation are provided in Table 2 within Appendix B.

Spectra are shown in Figure 2. In all cases narrow emission lines are observed from the LFBOT host galaxies, (e.g., Ca II H and K, [N II], [O II], [O III], and [S II]). The Balmer Hα line is prominent for all six objects. Spectra were obtained at the position of the transient (Figure 3) at a time when the transient and the host galaxy's brightness are comparable (Figure 1) so they typically contain contributions from both the transient and its host galaxy. All narrow emission lines we identified are well-known galactic emission lines; we do not identify any clear features from the transient itself, which is unsurprising given that at these phases LFBOT spectra are dominated by a blue continuum that is well approximated by a blackbody (e.g., R. Margutti et al. 2019; D. A. Perley et al. 2021).

2.3. Swift X-Ray Observations

X-ray observations were obtained with the Swift X-ray Telescope (XRT; D. N. Burrows et al. 2005) in the 0.3–10 keV range by Target of Opportunity (ToO) triggers shortly after discovery of each LFBOT. Count rates for the XRT instrument were obtained from the UKSSDC Swift light-curve generator.[37] Utilizing tools from NASA HEASARC, we converted these count rates to an X-ray flux accounting for the H I column density in the Milky Way. For upper limits (all objects except AT2024qfm), we assume a power-law photon index of $\Gamma = 2$, a typical value for previous LFBOTs (L. E. Rivera Sandoval et al. 2018; R. Margutti et al. 2019; J. S. Bright et al. 2022; D. Matthews et al. 2023).

For AT2024qfm, Swift obtained 12 observations, from $t_{\rm obs} \sim 8$–133 days after the first optical detection. We visually inspected the images and discarded one observation (ID 00016748006) because the source landed on the XRT detector's hot column. The X-ray light curve shows a general decline, with the exception of one observation (ID 00016748007), which showed a significant rebrightening. This observation was extremely short, with 233 s of raw exposure but only 40 s of clean data. Two source counts were detected at the position of AT2024qfm; using the R. P. Kraft et al. (1991) approach of the Swift tools, the implied detection significance is 99.83% (just over 3σ). Closer inspection of the data revealed no clear reason why this would be an erroneous measurement.

For purpose of comparison and for completeness, we also analyze three early Swift XRT observations of the LFBOT CSS161010. Late-time (100 days) observations were presented in D. L. Coppejans et al. (2020), while upper limits for these early observations were presented in C. P. Gutiérrez et al. (2024, see their Appendix A.1). We find a very marginal (3.3σ) detection in the first epoch, and nondetections in the subsequent two epochs. Our upper limits are within a factor of 3 of those in C. P. Gutiérrez et al. (2024), who presented binned measurements. We also show the 0.2–10 keV Chandra measurements of AT2023fhn published by A. A. Chrimes et al. (2024b), using the revised values in A. J. Nayana et al. (2025).

The Swift XRT observations are summarized in Table 3 in Appendix B. Five of the new LFBOTs had a Swift nondetection, resulting in upper limits for the photon count rate and the X-ray flux. These upper limits are compared to other objects with Swift detections in Figure 4.

2.4. Radio and Millimeter Observations

We obtained radio observations with the National Science Foundation's Karl G. Jansky Very Large Array (VLA; A. R. Thompson et al. 1980; R. A. Perley et al. 2011), the Giant Metrewave Radio Telescope (GMRT; G. Swarup et al. 1991), and the Northern Extended Millimeter Array (NOEMA). All of these observations are listed in Table 4 in Appendix B.

2.4.1. VLA

We present VLA observations for five LFBOTs,[38] all of which were detected. Radio data for AT2024qfm will be published by A. J. Nayana et al. (2026, in preparation) as per a prior arrangement. Observations were obtained at midfrequencies of 3 GHz (*S* band), 6 GHz (*C* band), 10 GHz (*X* band), 16 GHz (*Ku* band), and 33 GHz (*Ka* band). Based on the behavior of past sources (A. Y. Q. Ho et al. 2022b; Y. Yao et al. 2022; A. A. Chrimes et al. 2024a), 10 GHz (*X* band) gives the most reliable chances of detection, so every epoch features an observation in this band. We calibrate VLA data using the automated pipeline in Common Astronomy Software Applications (CASA) package version 6.5.4-9 (Team, T. C. et al. 2022). We use Briggs weighting with `robust = 0.5` (D. S. Briggs 1995). When the image quality is degraded by bright artifacts from nearby luminous sources, we perform phase-only self-calibration on these other sources. Flux measurements were determined by using the Cube Analysis

[35] SOAR2024B-021; PI: I. Andreoni.
[36] https://github.com/sncosmo/extinction
[37] UKSSDC Swift Light-Curve Generator

[38] AT2022abfc was observed under programs 22A-405 (PI: D. Perley), 23A-393, 23A-422, and 23B-138; AT2023fhn under programs 23A-403 and 23B-138; AT2023vth under program 23B-138; AT2023hkw under program 23A-415; and AT2024aehp under programs 24B-338 and 25A-367 (PI: A. Ho).

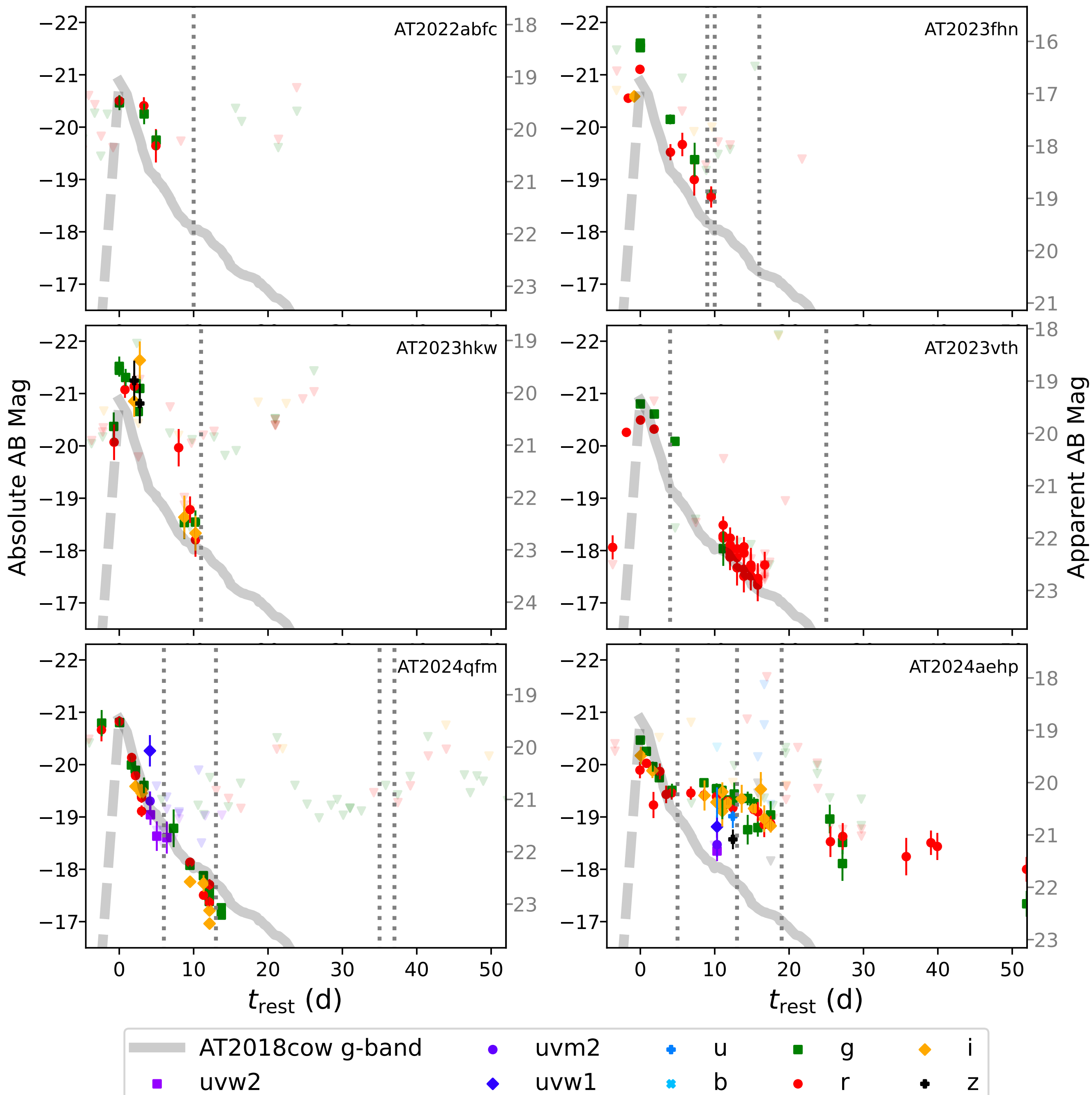

Figure 1. Optical light curves of each LFBOT (points), as well as the light curve of AT2018cow (thick gray line, where dashed lines mark the connection to the last upper limit). The left-hand ordinate values display the $E(B-V)$-corrected absolute AB magnitude (J. B. Oke & J. E. Gunn 1983) and are shared for all plots. The right-hand ordinate displays the apparent AB magnitude. Each filter has a unique marker color and style. Upside-down triangles represent 3σ upper limits. The vertical dotted lines show when spectra of the transient and/or its host galaxy were taken. These spectra are displayed in Figure 2.

and Rendering Tool (A. Comrie et al. 2021). For detections, the flux density is the maximum intensity at the transient's position, and the uncertainty is the measured rms in the background. For nondetections, we take the upper limit to be 3 × rms. The radio light curves are shown in Figure 5 and the radio SED evolution is shown in Figure 6.

2.4.2. GMRT

We also present GMRT observations of AT2022abfc, AT2023fhn, AT2023hkw, and AT2023vth. Both AT2023fhn and AT2023vth were detected. These observations were spread across three frequency bands: Band 3 (250–500 MHz), Band 4 (550–850 MHz), and Band 5 (1000–1460 MHz).[39] The GMRT data were reduced through CASA and AIPS. We use Briggs weighting with `robust = 0.5`. The primary beam correction was done following the method described in the CASA documentation.[40] We measure the flux density using the `imfit` method in the CASA documentation, which provides the maximum intensity for a fitted Gaussian. If the measured

[39] AT2022abfc was observed under program ID 44_099. AT2023fhn was observed under programs 45_117 and ddtC299. AT2023hkw was observed under 45_117 and ddtC294. AT2023vth was observed under program 45_113 (PI: A. J. Nayana).

[40] CASA: Imaging with Custom Primary Beams

flux is not 3σ above the background flux rms, we record an upper limit of $3\times$ the rms.

2.4.3. NOEMA

We observed five LFBOTs using NOEMA[41] (all but AT2023hkw), at times ranging from $t = 10$–100 days, resulting in detections of three objects (AT2024aehp, AT2024qfm, and AT2023vth) and nondetections of two objects (AT2022abfc and AT2023fhn). The data reduction was done with Continuum and Line Interferometer Calibration and `MAPPING`, which are part of the `GILDAS` software package (Gildas Team 2013).[42] Unless otherwise specified, all uncertainties are 1σ, and the systematic error of the flux scale is 10% in the 3 mm band and 15% at 1.3 mm. The NOEMA data are provided in Table 4 and displayed in Figure 7.

AT2024aehp was observed on 2025 May 23 (>100 days after optical discovery; we triggered millimeter observations following the centimeter-wave detection) in the 10D configuration under mediocre weather conditions, with MWC349 as the flux calibrator. Reduction was performed by hand and we estimate a 15% systematic calibration uncertainty for the absolute flux scale.

AT2023fhn was observed on 2023 April 22 in the 12C configuration under good conditions, with LKHA101 as the flux calibrator. The image included a nearby bright source, and subtracting the contribution from the bright source did not result in a detection of AT2023fhn at the phase center.

An observation of AT2022abfc was triggered on 2022 December 30; an attempt was made on 2023 January 7, but could not be carried out owing to bad weather. A successful observation was obtained on January 10 in the 12A configuration, with LKAH101 as the flux calibrator. The source was not detected, but limits were weak because the source was at high airmass and the array was in an extended configuration.

AT2023vth was first observed on 2023 November 20 in the 9C configuration, under cloudy conditions, with the flux calibrator MWC349. The source was detected, so we pursued multifrequency follow-up observations. The timing of these observations was affected by weather conditions, particularly at the highest frequencies.

NOEMA observed AT2024qfm on four dates, in compact configuration (D), with primary flux calibrator MWC349. The first observation was on 2024 August 5. The source was detected in the first three epochs.

2.5. Search for Gamma-Ray Bursts

We performed an archival search for GRB detections in the NASA General Coordinates Network Circulars.[43] We looked for GRBs detected within a week of the transient's optical light-curve peak that had a localization that was within 3σ of the transient's coordinates. No such GRBs were reported.

2.6. Search for X-Ray Precursors

One way to distinguish between LFBOT progenitor models could be to detect precursor emission: this might be expected in a model with runaway mass transfer leading up to the dynamical merger of a stripped star and compact-object companion (B. D. Metzger 2022; D. Tsuna et al. 2024) but not in, e.g., a core-collapse scenario. We searched for X-ray precursor emission in the eROSITA-DE Data Release 1 (DR1). eROSITA (P. Predehl et al. 2021) is the soft X-ray instrument on board the orbital observatory Spectrum-Roentgen-Gamma (SRG; R. Sunyaev et al. 2021). DR1 comprises data from the first 6 months, which ended in 2020 June (A. Merloni et al. 2024; D. Tubín-Arenas et al. 2024).

Of the 13 LFBOTs in Table 1, three were in the footprint of eROSITA-DE DR1: AT2022abfc, CSS161010, and AT2024wpp. For each object, we used the products from D. Tubín-Arenas et al. (2024) and A. Merloni et al. (2024) to determine if there was a detection at the source position, and if not, obtained a 0.2–2.3 keV upper limit (the most sensitive energy range for eROSITA). As each field was only imaged once in this data release, we only check for consistency in position and allow the observation to be at any time. The closest cataloged sources were offset by 5.5′ (AT2022abfc), 3′ (CSS161010), and 2′ (AT2024wpp), too distant to be associated (the spatial resolution of eROSITA is <10″; P. Predehl et al. 2021).

For AT2022abfc and AT2024wpp (the two objects for which the eROSITA observations were prior to the LFBOT), the limits are 9.1×10^{42} erg s^{-1} corresponding to 2.7 yr pre-LFBOT, and 9.0×10^{41} erg s^{-1} corresponding to 4.7 yr pre-LFBOT, respectively. For CSS161010, the eROSITA limit is 1.5×10^{41} erg s^{-1}, 3.4 yr after the LFBOT. The next eROSITA data release (scheduled for mid-2026) will provide more stringent upper limits (i.e., closer to the LFBOT time).

2.7. Host-galaxy Photometry

IR and UV photometry were obtained for all LFBOT host galaxies from the Near-Earth Object Wide-field Infrared Survey Explorer (NEOWISE) mission (A. Mainzer et al. 2011) on the Wide-field Infrared Survey Explorer (WISE) space telescope, and the Galaxy Evolution Explorer (GALEX; D. C. Martin et al. 2005), respectively. Optical photometry for the host galaxies was obtained from the Legacy Survey Data Release 10 (A. Dey et al. 2019). The host galaxy of AT2023vth does not have Legacy Survey optical photometry, so we used optical photometry from Pan-STARRS1 (PS1) Data Release 2 (DR2; K. C. Chambers et al. 2016; H. A. Flewelling et al. 2020). We also used Hubble Space Telescope (HST) photometry from A. A. Chrimes et al. (2024b) for AT2023fhn. All the GALEX data used in this paper can be found in MAST at DOI: 10.17909/zktz-mn64. For the photometry in all bands, we required a signal-to-noise ratio (SNR) greater than five for a detection. We choose this SNR to include several marginal GALEX and WISE detections, while excluding a few measurements with errors of over 0.5 mag. Choosing a stricter cutoff would make the fit far more uncertain as we lose a significant number of data points, but a looser cutoff would have little effect as the new points would have large errors, which the fitting process accounts for. We display cutouts of the host galaxies in Figure 3

We used the Python package `gPhoton` (C. Million et al. 2016) to retrieve GALEX near-UV and far-UV photometry for the LFBOT host galaxies. In `gPhoton`, we chose the observation with the longest exposure time and recorded the background-corrected magnitudes. We chose an aperture radius of 6.″12 for the source, and measured the background

[41] Program IDs W22BT (AT2023fhn and AT2022abfc), W24EW (AT2024aehp), S23BF (AT2023vth), and D24AA (Director's Discretionary Time; AT2024qfm); all with PI: A. Ho.

[42] https://www.iram.fr/IRAMFR/GILDAS

[43] https://gcn.nasa.gov/circulars/

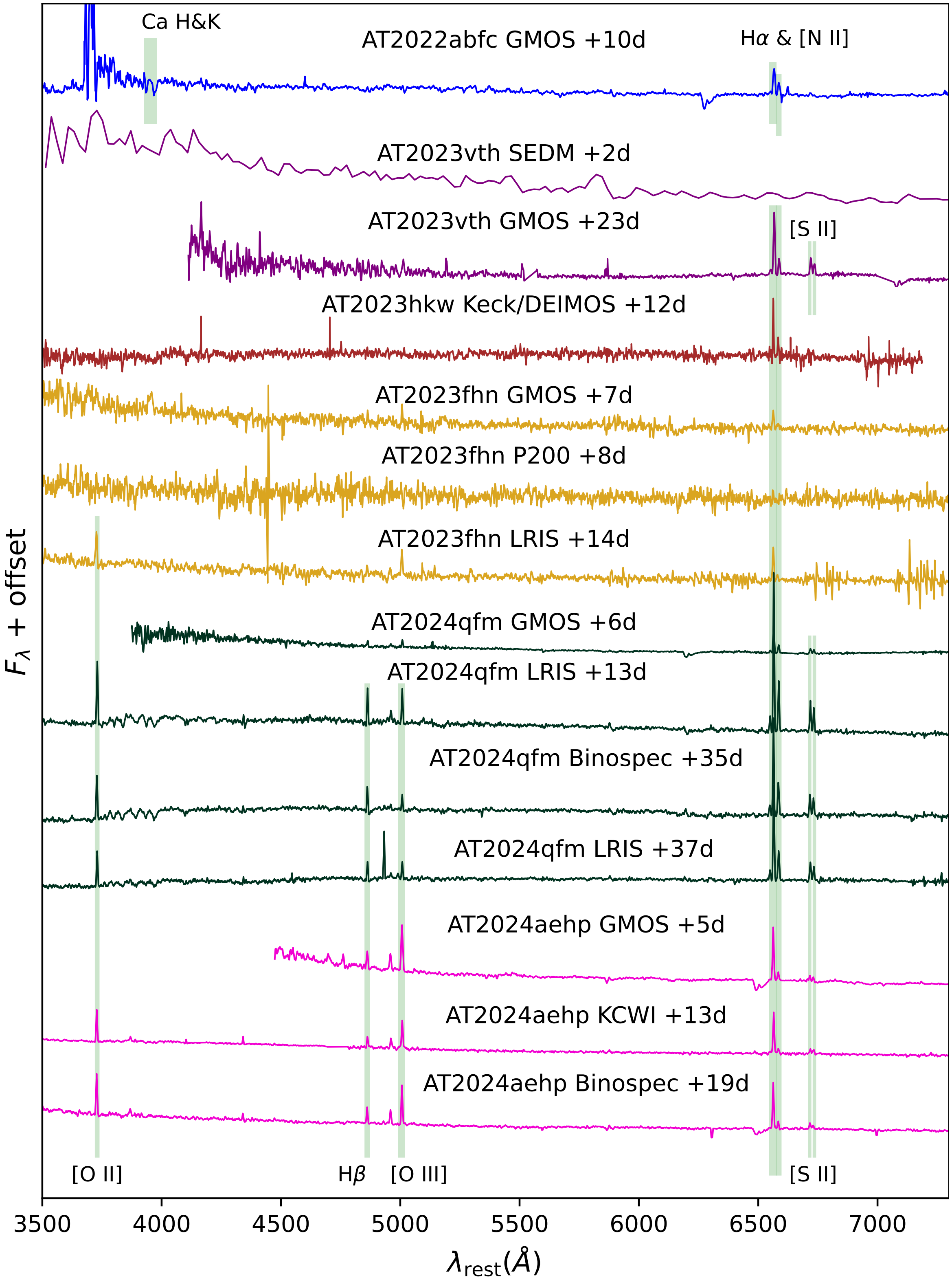

Figure 2. Spectra of each LFBOT and/or its host galaxy. For each spectrum we indicate the observer-frame epoch and instrument used. We bin all spectra with a bin size of 3 Å. The green shaded rectangles show galactic narrow emission lines that were used to determine a redshift. The spectra are displayed with an arbitrary vertical offset.

from an annulus with an inner radius of 10.″8 and an outer radius of 21.″6. We estimate that this size would exclude all of the host galaxy's emission and include as much background as possible for an accurate background flux estimate without including any flux from other sources. We apply this annulus size to most of the LFBOT hosts to maintain consistency. In the cases of AT2023hkw and AT2023vth, there were nearby UV-bright sources that required us to use a smaller annulus. The inner and outer annulus radii are 10.″8 and 16.″2 for AT2023hkw, and 7.″2 and 10.″8 for AT2023vth. Legacy

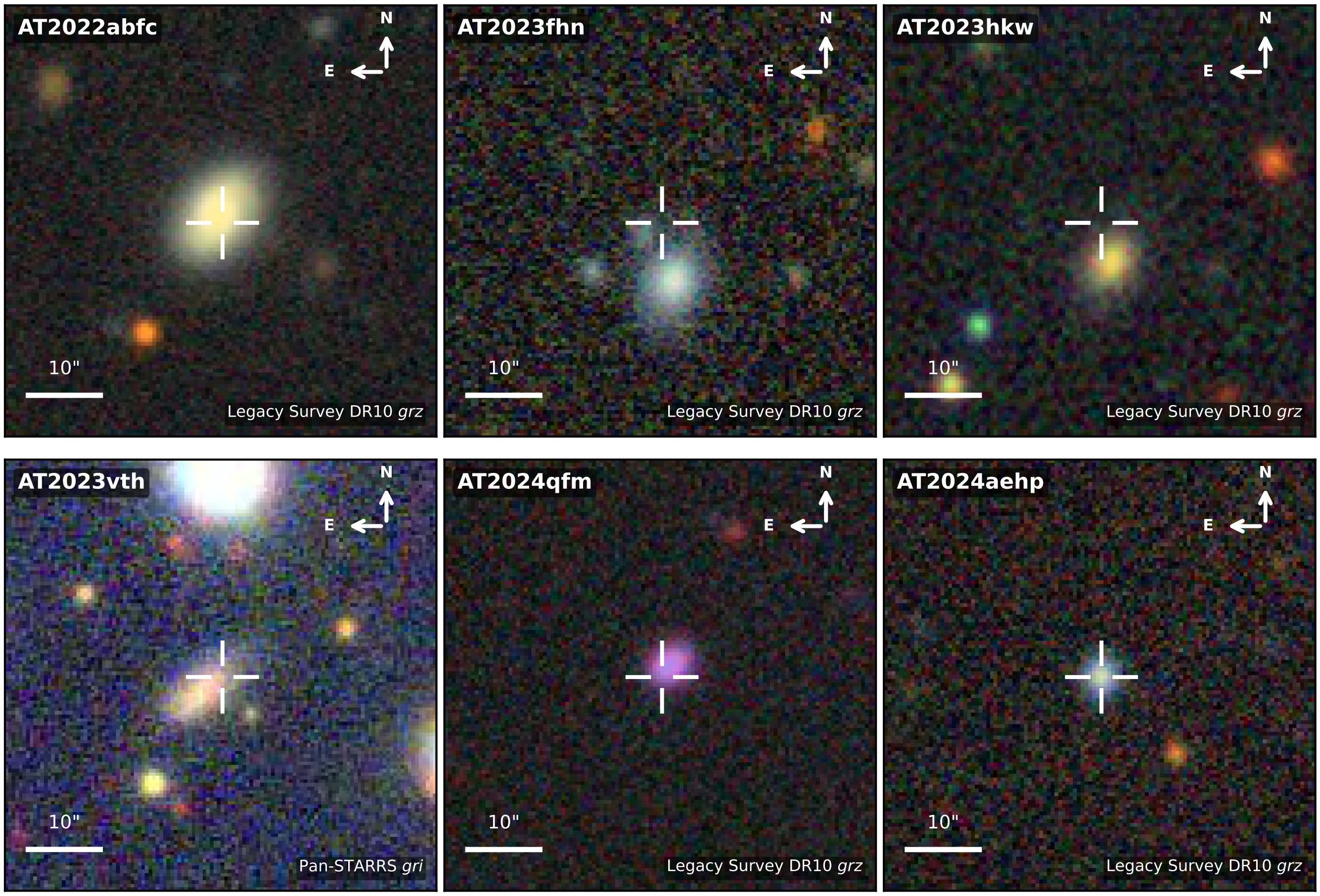

Figure 3. Optical cutouts of the six LFBOT host galaxies we discuss in this paper. In each panel we mark the position of the LFBOT with cross hairs.

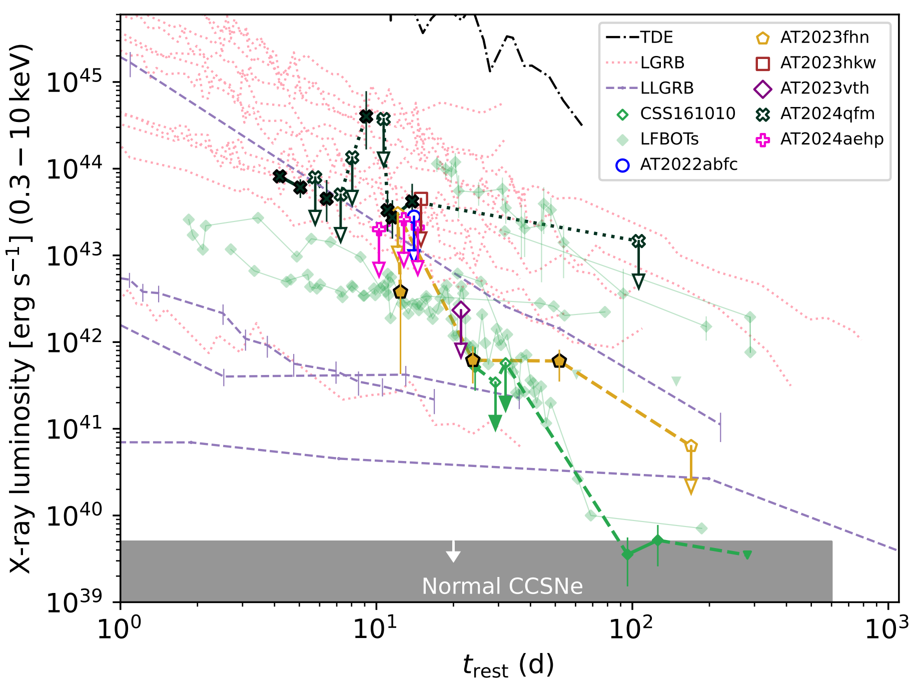

Figure 4. 0.3–10 keV X-ray light curves of the six LFBOTs in this paper, in comparison to those of other LFBOTs, long GRBs (LGRBs), and low-luminosity GRBs (LLGRBs). Open symbols with downward-facing triangles mark 3σ upper limits. Data are from E. Pian et al. (2000), A. Tiengo et al. (2004), S. Campana et al. (2006), A. M. Soderberg et al. (2006b), P. K. Blanchard et al. (2017), A. Y. Q. Ho et al. (2020b), D. L. Coppejans et al. (2020), J. T. Hinkle et al. (2021), D. A. Perley et al. (2021), Y. Yao et al. (2022), A. Y. Q. Ho et al. (2022c), D. Perley (2023), A. Y. Q. Ho et al. (2023c), A. A. Chrimes et al. (2024a), Y. Yao et al. (2024), and D. A. Perley et al. (2026), as well as public Swift data.

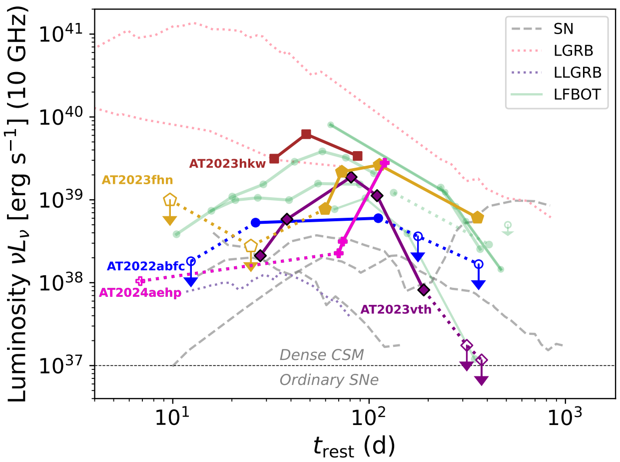

Figure 5. Radio light curves at 10 GHz of the LFBOTs with data presented in this paper, compared with other known LFBOTs, LGRBs, LLGRBs, and core-collapse supernovae (CCSNe) with nonrelativistic ejecta. We measure time after peak light in the transient's rest frame. Data from S. R. Kulkarni et al. (1998), E. Berger et al. (2003), A. M. Soderberg et al. (2006a), A. J. van der Horst et al. (2008), A. M. Soderberg et al. (2010b), P. Salas et al. (2013), R. Margutti et al. (2019), D. L. Coppejans et al. (2020), A. Y. Q. Ho et al. (2022b), Y. Yao et al. (2022), D. A. Perley et al. (2021), A. Y. Q. Ho et al. (2023c), and A. J. Nayana et al. (2025).

Survey and NEOWISE photometry was obtained with the Python package `noaodatalab`[44] version 2.20.0. PS1 DR2 *grizy* photometry was retrieved through the online catalog search tool.[45]

The host-galaxy photometry is provided in Table 5 in Appendix B.

3. Radio Analysis

3.1. Radio Synchrotron Modeling

We model the SED at radio and millimeter wavelengths as the result of synchrotron emission. Synchrotron radiation with a self-absorbed component forms a broken power-law radio SED. We follow the prescription of R. A. Chevalier (1998) to derive properties of the shock and the medium it traverses, such as the shock radius, ambient magnetic field, average shock velocity, preshock density, and total shock energy. This is the same procedure used in modeling the radio SEDs for other AT2018cow-like FBOTs (e.g., A. Y. Q. Ho et al. 2019; R. Margutti et al. 2019; A. A. Chrimes et al. 2024b; A. J. Nayana et al. 2025; D. A. Perley et al. 2026). We note that in some of these works, some equations are given in terms of angular diameter distance D_θ, but should be given in terms of luminosity distance (D_L; B. Margalit 2026, private communication) as in the expressions below. We also note that the following prescription assumes a nonrelativistic shock and does not account for relativistic effects (see, e.g., B. Margalit & E. Quataert 2024; R. Ferguson & B. Margalit 2026), which become relevant for $\Gamma\beta \sim 1$. For self-consistency, we estimate the $\Gamma\beta$ this model outputs and we find that some objects do approach the transrelativistic regime (Figure 8), so we caution against taking our presented results at face value for the higher-velocity events. Still, we use this method for comparison with previous LFBOTs, which is the main goal of this paper's analysis.

[44] https://github.com/astro-datalab/datalab
[45] https://catalogs.mast.stsci.edu/panstarrs/

As in A. M. Soderberg et al. (2010a), we assume equipartition of energy between protons, electrons, and the magnetic field; thus, the energy densities in electrons (ϵ_e) and magnetic fields (ϵ_B) are given by $\epsilon_e = \epsilon_B = 1/3$. If we model the source of the emission as a disk with radius R and thickness S, then its total volume is $\pi R^2 S$. We then parameterize this as equivalent to a spherical volume of $4\pi f R^3/3$, where f is the filling factor. We take $f = 0.5$ as in previous LFBOT studies (J. S. Bright et al. 2022; Y. Yao et al. 2022), but the dependences of the equations on this parameter are weak. We assume an electron power-law index of 3, following R. A. Chevalier & C. Fransson (2006); this is a typical value for previous LFBOTs as determined from fits to the slope of the self-absorbed end of the synchrotron SED (A. Y. Q. Ho et al. 2019; D. L. Coppejans et al. 2020). We do not have more than two points in the self-absorbed regime for most of our SEDs, so we use this fiducial value with the recognition that the results do not strongly depend on the optically thin power-law index (R. A. Chevalier 1998).

Finally, we verify that the self-absorption frequency is less than the cooling frequency, which is defined as the frequency where the electrons have lost an amount of energy equal to their total energy through synchrotron cooling. We use Equation (C13) of A. Y. Q. Ho et al. (2022b), which gives the ratio between the self-absorption and cooling frequencies, and confirm that the self-absorption frequency is lower for all cases.

Under these assumptions, Equations (13) and (14) from R. A. Chevalier (1998) reduce to these expressions for the shock radius and magnetic field:

$$R_{\rm p} = 8.8 \times 10^{15} \left(\frac{\epsilon_e}{\epsilon_B}\right)^{-1/19} \left(\frac{f}{0.5}\right)^{-1/19} \left(\frac{F_{\rm p}}{(1+z)\ {\rm Jy}}\right)^{9/19} \times \left(\frac{D_L}{\rm Mpc}\right)^{18/19} \left(\frac{\nu_{\rm p}}{5\ {\rm GHz}}\right)^{-1} {\rm cm}\,, \quad (2)$$

$$B = 0.58 \left(\frac{\epsilon_e}{\epsilon_B}\right)^{-4/19} \left(\frac{f}{0.5}\right)^{-4/19} \left(\frac{F_{\rm p}}{(1+z)\ {\rm Jy}}\right)^{-2/19} \times \left(\frac{D_L}{\rm Mpc}\right)^{-4/19} \left(\frac{\nu_{\rm p}}{5\ {\rm GHz}}\right) {\rm G}\,, \quad (3)$$

where D_L is the luminosity distance, and $\nu_{\rm p}$ and $F_{\rm p}$ are the peak frequency and flux density at peak frequency of the radio SED in the transient's rest frame, respectively.

Following A. Y. Q. Ho et al. (2019), these can then be combined into an equation for total energy $U = U_B/\epsilon_B$:

$$U = \frac{B^2}{8\pi} \frac{4\pi f R^3}{3} \frac{1}{\epsilon_B} = 1.9 \times 10^{46} \left(\frac{1}{\epsilon_B}\right) \left(\frac{\epsilon_e}{\epsilon_B}\right)^{-11/19} \left(\frac{f}{0.5}\right)^{8/19} \times \left(\frac{F_{\rm p}}{(1+z)\ {\rm Jy}}\right)^{23/19} \left(\frac{D_L}{\rm Mpc}\right)^{46/19} \left(\frac{\nu_{\rm p}}{5\ {\rm GHz}}\right)^{-1} {\rm erg}\,. \quad (4)$$

We estimate the average velocity as $R/(t_{\rm obs}/(1+z)) = R/t_{\rm rest} = \Gamma\beta c$, where $\beta = v/c$ and Γ is the Lorentz factor.

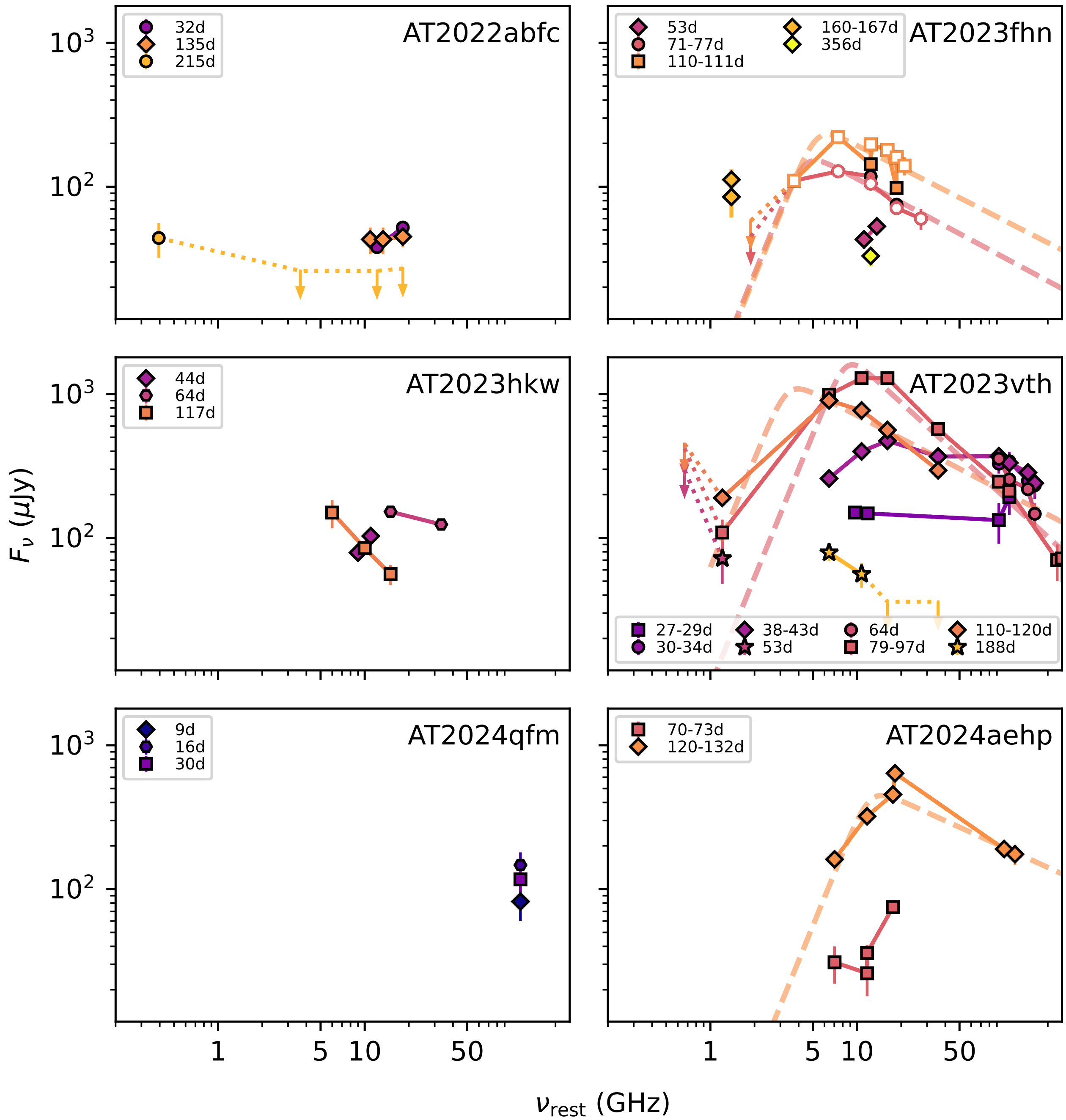

Figure 6. The radio and millimeter SED of each LFBOT at different observer-frame epochs. Observations taken within a few days are grouped into one epoch. Nondetections are signified by a downward-pointing arrow. For clarity, we omit some nondetections. For epochs with sufficient data points, we display the broken power-law fit to the SED as a dashed line. Data from A. A. Chrimes et al. (2024a) for AT2023fhn have markers filled in with white.

Following A. A. Chrimes et al. (2024b), we derive formulas for the circumstellar medium (CSM) electron number density n_e and the wind density $\dot{M}/v_{\rm w}$. This assumes the CSM resulted from a spherical stellar wind with mass-loss rate $\dot{M}$ and wind velocity $v_{\rm w}$, where $\dot{M}/v_{\rm w} = 4\pi m_p R^2 n_e$ and m_p is the proton mass. Thus

$$n_e = 1.02 \frac{1}{\epsilon_B}\left(\frac{\epsilon_e}{\epsilon_B}\right)^{-6/19}\left(\frac{f}{0.5}\right)^{-6/19}\left(\frac{F_{\rm p}}{(1+z)\ {\rm Jy}}\right)^{-22/19} \times \left(\frac{D_L}{\rm Mpc}\right)^{-44/19}\left(\frac{\nu_{\rm p}}{5\ {\rm GHz}}\right)^{4}\left(\frac{t_{\rm rest}}{\rm days}\right)^{2} {\rm cm}^{-3}, \quad (5)$$

$$\frac{\dot{M}}{v_{\rm w}}\left(\frac{1000\ {\rm km\ s^{-1}}}{10^{-4}\ M_\odot\ {\rm yr^{-1}}}\right) = 2.5 \times 10^{-5}\left(\frac{1}{\epsilon_B}\right)\left(\frac{\epsilon_e}{\epsilon_B}\right)^{-8/19} \times \left(\frac{f}{0.5}\right)^{-8/19}\left(\frac{F_{\rm p}}{(1+z)\ {\rm Jy}}\right)^{-4/19} \times \left(\frac{D_L}{\rm Mpc}\right)^{-8/19}\left(\frac{\nu_{\rm p}}{5\ {\rm GHz}}\right)^{2} \times \left(\frac{t_{\rm rest}}{\rm days}\right)^{2}. \quad (6)$$

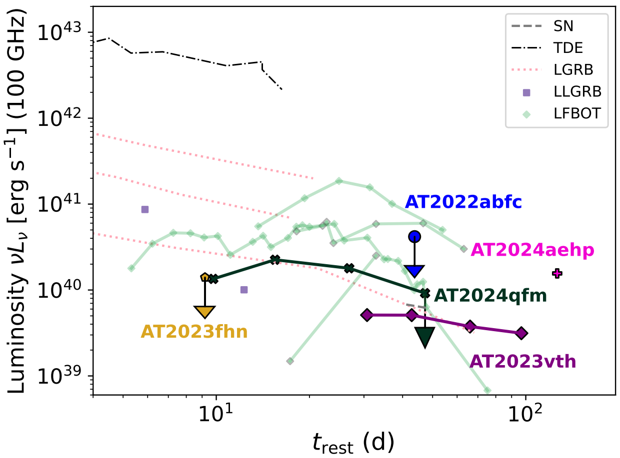

Figure 7. Millimeter-wave (100 GHz) light curves in comparison to other LFBOTs, LGRBs, LLGRBs, and TDEs. AT2022abfc and AT2023fhn only have an upper limit. AT2023fhn has been shifted slightly to the left for clarity. Data are from S. R. Kulkarni et al. (1998), B. A. Zauderer et al. (2011), D. A. Perley (2013), A. Corsi et al. (2014), T. Laskar et al. (2016), D. A. Perley et al. (2017), T. Laskar et al. (2018), R. Margutti et al. (2019), J. S. Bright et al. (2022), A. Y. Q. Ho et al. (2023c), and A. J. Nayana et al. (2025).

The peak frequency and flux density of the SED at a given epoch are measured by fitting a smoothed broken power law of the form

$$F(\nu) = F_{\rm p}\left((\nu/\nu_{\rm p})^{-sa_1} + (\nu/\nu_{\rm p})^{-sa_2}\right)^{-1/s}. \quad (7)$$

We choose $s = 1$ for the smoothness parameter, as was done in previous LFBOT studies (J. S. Bright et al. 2022; A. A. Chrimes et al. 2024a; A. J. Nayana et al. 2025). We also set $a_1 = 5/2$ to fix the power-law slope of the self-absorbed half of the SED, as required by R. A. Chevalier (1998)'s formulation. When an epoch involves observations from multiple observatories, we apply an extra error in quadrature equal to 10% of the flux density to account for systematic effects between arrays. A fit is performed only when we have detections on either side of the SED's peak. The best-fit parameters from the broken power-law fit are provided in Table 7 in Appendix B. If we are unable to perform a broken power-law fit, we use the values at the detection closest to the peak's implied location in place of the frequency and flux density at peak, and calculations based on these values will instead set limits on the synchrotron parameters. The inferred synchrotron parameters are listed in Table 8 in Appendix B, and the results are displayed in Figure 8. These include epochs where we do fit a broken power law and have point estimates for parameters, and epochs where we can only constrain the peak's location and place limits on parameters instead. We find that the implied CSM densities for these six LFBOTs are comparable to those derived in the literature for previous LFBOTs, with values of 10–100 cm^{-3} at radii of 10^{17} cm.

4. Host-galaxy Analysis

4.1. Host-galaxy Offsets

With an expanded sample of 13 LFBOTs (double the previous size in the literature), we also examine the distribution of LFBOT offsets from the host-galaxy nuclei. We choose the host galaxy as the galaxy closest in offset to the transient, and then confirm that there are no lines at conflicting redshifts in spectroscopy of the LFBOT and its host. To measure offsets, we require accurate localizations of each LFBOT and its host galaxy. For AT2023fhn and its host, we used the localization from HST imaging presented by A. A. Chrimes et al. (2024b). For the other LFBOTs, we measure the host galaxy's position from Legacy Survey Data Release 10, and the transient's position from a Gaussian fit in the image of the LFBOT's brightest radio detection. We also do this for AT2020xnd, which did not have a published offset. The exceptions are AT2023vth's host (which was measured from the PS1 DR2), and AT2024qfm's localization which we measure from the ZTF data (as we do not present AT2024qfm's radio data in this paper). These offsets are recorded in Table 1.

In Figure 9, we display the cumulative distribution of all LFBOT offsets in kiloparsecs compared with other classes of extragalactic explosive transients. The offset distribution appears to be intermediate to that of CCSNe and that of LGRBs and superluminous supernovae (SLSNe).

4.2. Host-galaxy Properties

We used the Python package `prospector` (J. Leja et al. 2017; B. D. Johnson et al. 2021)[46] to derive properties such as stellar mass and star formation rate (SFR) from the host-galaxy photometry. The `prospector` package utilizes the Flexible Stellar Population Synthesis[47] (FSPS) package to model the emission from each galaxy given a set of parameters for the galaxy's composition and stellar population. It also utilizes dynamic nested sampling through the package `dynesty`[48] to fit galaxy parameters to the observed galaxy photometry under Bayesian inference. The basic parametric star formation history (SFH) template is adopted along with the parameters for nebular emission. We chose the Chabrier initial mass function (G. Chabrier 2003), the Calzetti dust attenuation model (D. Calzetti et al. 2000), and a SFH of the form $te^{-t/\tau}$. These procedures were chosen to match LFBOT host-galaxy analysis in previous papers as closely as possible (Y. Yao et al. 2022; A. Y. Q. Ho et al. 2023c; A. A. Chrimes et al. 2024a). A model was first run with a fixed metallicity of $\log(Z/Z_\odot) = -0.2$. Then, we used the median mass and the mass–metallicity relation of A. Gallazzi et al. (2005) to fix the metallicity to a more accurate value, and ran a final model. The fitted parameters are listed in Table 5, the best-fit photometry and spectroscopy are displayed in Figure 10, and the fitted host-galaxy properties are listed in Table 6. We show the median host-galaxy masses and SFRs in Figure 11. Our host-galaxy properties derived for the host of AT2023fhn agree with A. A. Chrimes et al. (2024a) to within 1σ for the host-galaxy mass and 2σ for the SFR.

The host galaxies of our LFBOTs are all star-forming galaxies. Whereas several previous events were in low-mass dwarf galaxies (R. Margutti et al. 2019; D. L. Coppejans et al. 2020; A. Y. Q. Ho et al. 2020a; A. A. Chrimes et al. 2024b), the host galaxies of four of our new LFBOTs have higher masses (10^{10}–10^{11} $M_\odot$, Figure 11). However, our selection criteria for identifying LFBOT candidates do require there to be a visible host galaxy (to avoid contamination by dwarf novae), so a bias to higher-mass galaxies (and therefore higher SFR) is to be expected.

[46] https://github.com/bd-j/prospector
[47] https://dfm.io/python-fsps/current/
[48] https://github.com/joshspeagle/dynesty

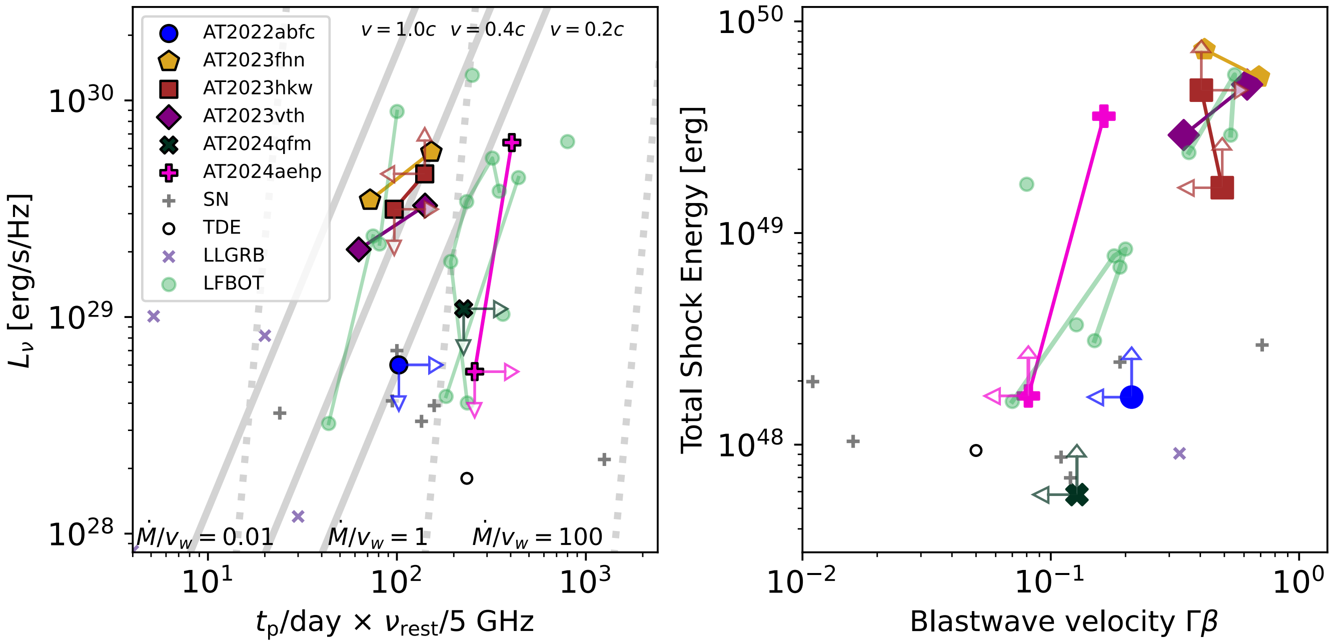

Figure 8. Inferred parameters from our synchrotron self-absorption modeling. Some epochs do not include the self-absorption peak and merely constrain its location; the corresponding upper limits on parameters are marked with arrows. Values for other objects are obtained from A. Y. Q. Ho et al. (2019) and A. Y. Q. Ho et al. (2023c); and D. A. Perley et al. (2026) for AT2024wpp. We label each object and the observer-frame time after peak light. Left: luminosity density at ν_p vs. peak frequency and time after explosion. We also display lines of constant shock velocity and $\dot{M}/v_w$, where $v_w = 1000$ km s^{-1} and $\dot{M}$ is in units of $10^{-4}\,M_\odot$ yr^{-1}. Right: total shock energy derived from Equation 4 against shock velocity in terms of $\Gamma\beta$.

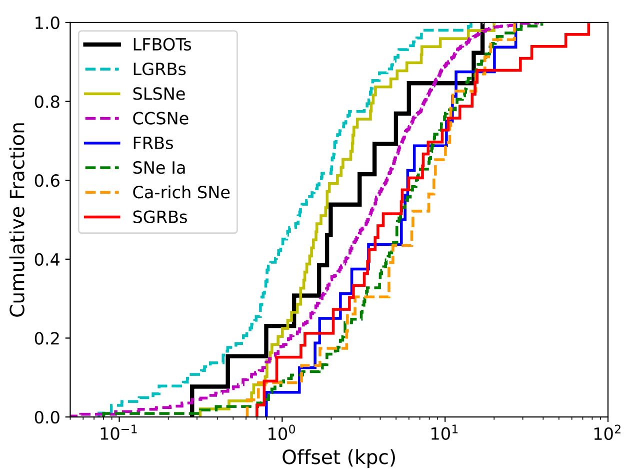

Figure 9. The cumulative distribution of host-galaxy offsets for LFBOTs, as well as fast radio bursts (S. Bhandari et al. 2022), LGRBs (P. K. Blanchard et al. 2016; J. D. Lyman et al. 2017), short GRBs (W.-f. Fong et al. 2022), CCSNe (P. L. Kelly & R. P. Kirshner 2012; S. Schulze et al. 2021), Type Ia SNe (X. Wang et al. 2013), SLSNe (R. Lunnan et al. 2015; S. Schulze et al. 2021), and Ca-rich transients (K. De et al. 2020). The offsets for previous LFBOTs are from S. J. Prentice et al. (2018), D. L. Coppejans et al. (2020), A. Y. Q. Ho et al. (2020a), Y. Yao et al. (2022), and A. A. Chrimes et al. (2024b).

To compare the intrinsic distribution of host-galaxy mass to that of CCSNe, we used the untargeted sample of 150 CCSN host galaxies from K. Taggart & D. A. Perley (2021) as representative of the true CCSN host-galaxy population. We prioritized having an unbiased sample over a large comparison sample, as our uncertainties are limited by our small LFBOT sample. For each of the 13 LFBOT host galaxies, we calculate the minimum absolute magnitude for it to have been detected by the Legacy Survey at that redshift, which corresponds to the apparent magnitude cutoff of $m_r \leqslant 23$. Then, for each CCSN host galaxy, we apply a weight equal to the proportion of the 13 cutoffs that the CCSN host galaxy would pass. We do not account for any systematic differences in host-galaxy properties between those at redshift $z \approx 0.01$ as in the K. Taggart & D. A. Perley (2021) sample, and those at $z \approx 0.1$–0.2 as with most of the LFBOTs. We plot the Gaussian kernel density estimation (KDE) for the weighted distribution of CCSN host-galaxy masses in Figure 12 as a dotted red line. The Gaussian KDE for the LFBOT host-galaxy masses is shown in black. We repeated the exercise for SLSNe, which are known to have a preference for lower galaxy masses than regular CCSNe (K. Taggart & D. A. Perley 2021).

We use the `Ecume` package (H. Roux de Bezieux 2024) in the programming language R (R Core Team 2025) to perform a KS test comparing the distribution of LFBOT host-galaxy masses with the weighted CCSN and SLSN populations. These simulations imply that the LFBOT host-galaxy population is consistent with both the populations of CCSN and SLSN host galaxies at a significance of $\alpha = 0.05$ (which means that the p-value must be less than 0.05 for us to conclude that the underlying distributions are different with 95% confidence). We also display the results of the KS test in Figure 12. The SLSN host-galaxy distributions appears especially similar to that of LFBOTs. However, the SLSNe are subdivided into SLSNe-I and SLSNe-II. These two classes are markedly different, and this is reflected in their host-galaxy masses—SLSN-I host galaxies are clustered around $\log(M/M_\odot) \approx 8$ while SLSN-II hosts are $\log(M/M_\odot) \approx 9$–10. Despite the visible differences, the sample sizes of SLSN-I and SLSN-II hosts are too small to find a statistically significant difference at $\alpha = 0.05$.

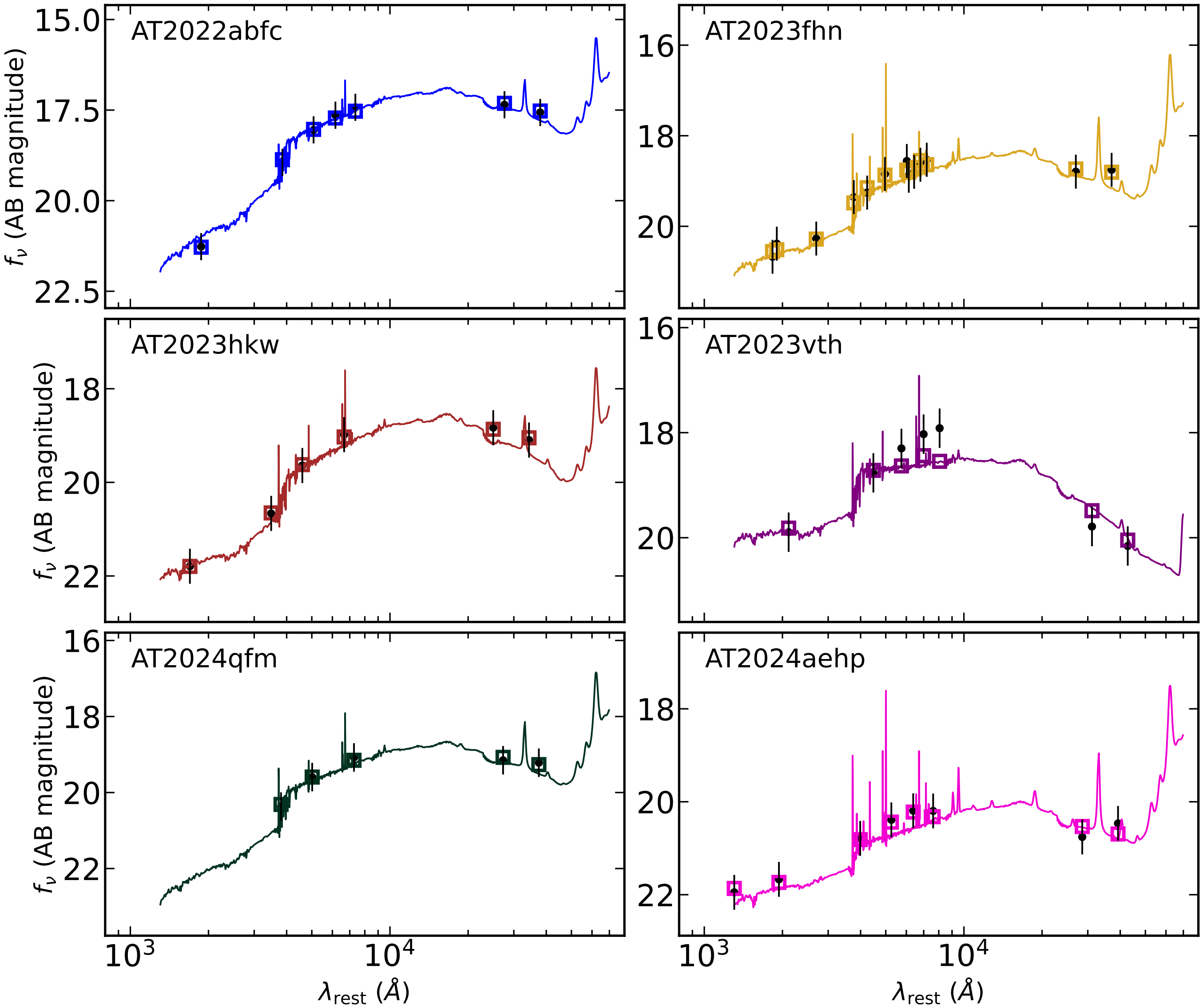

Figure 10. Best-fit host-galaxy spectra and photometry from `prospector` (color) as well as the input photometry (black circles with error bars). Note that the parameters reported in Table 6 are the median, 16th percentile, and 84th percentile. The best-fit host-galaxy spectra displayed here corresponds to the maximum a posteriori model, which may not necessarily have the median parameters. The abscissa displays rest-frame wavelength.

5. Discussion

5.1. Observational Comparison

The objects presented in Section 2 show relative homogeneity in the optical (Figure 1) and radio (Figure 5) light curves. To some extent the similarity of the optical light curves to those of AT2018cow is by selection, as these objects were identified on the basis of a rapid rise and decay within the 2–3 days of the optical peak, along with high luminosities. The rapid decline of 3–4 mag over $t_{\rm rest} \approx 10-15$ days observed in AT2023fhn, AT2023vth, AT2023hkw, and AT2024qfm—very similar to AT2018cow—was not selected for. We note that AT2024aehp differs in many of these properties. This section will focus on the other LFBOTs in our sample; AT2024aehp will be discussed in more detail in Section 5.3.

While the other optical light curves could appear similar due to selection effects, selection effects do not account for the similarity between the LFBOT radio light curves as we only require one detection for classification. Figure 5 shows that the peak νL_ν values mostly lie within the range of 10^{39}–10^{40} erg s^{-1}. The time evolution for the radio emission is also similar across the sample. The 10 GHz luminosity gradually rises, plateaus between $t_{\rm rest} \sim 50$–100 days after the initial discovery, and then begins to fade. During the rise, the radio emission is typically optically thick (has a positive spectral index; Figure 6). The decay rates of the radio emission vary, and in some cases are poorly constrained (e.g., for AT2022abfc). The fast fade of AT2023vth is similar to that of CSS161010 (D. L. Coppejans et al. 2020). Meanwhile, the millimeter-wave light curves appear to peak close at times close to $t_{\rm rest} = 20-30$ days (Figure 7). All SEDs either have or are consistent with a broken power-law shape. The frequency is near 50 GHz during the first detections at $t_{\rm rest} \sim 30$ days, then gradually shift to lower frequencies, passing 10 GHz at roughly $t_{\rm rest} \sim 100$ days.

The uniformity of the radio luminosity and evolution of all AT2018cow-like FBOTs is striking. Of course, the radio emission had to be sufficiently luminous to be detected in the first place, but we did not require the radio luminosity to brighten over time, nor was there a requirement about the

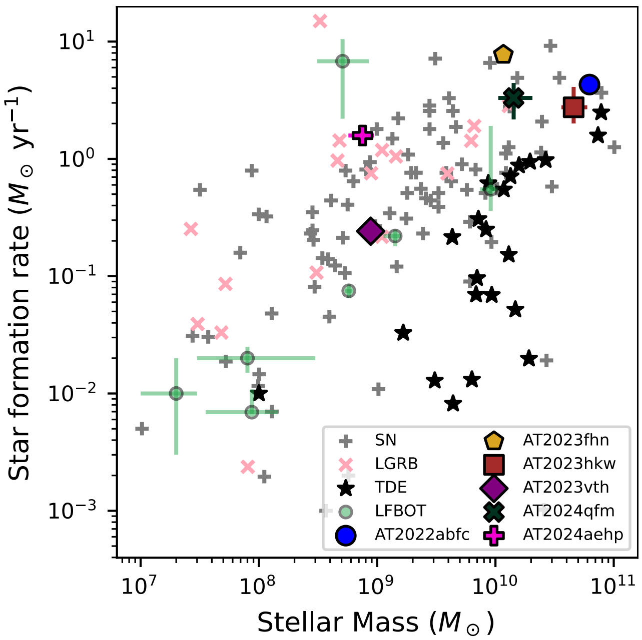

Figure 11. Median mass and SFR for each LFBOT's host galaxy in comparison to the host galaxies of other energetic transients. Colored lines show error bars, though they may be smaller than the marker for some points. Data for the other transients from J. Law-Smith et al. (2017), K. D. French et al. (2020), K. Taggart & D. A. Perley (2021), and J. J. Somalwar et al. (2025).

timing of the peak. The radio behavior is in sharp contrast to CCSN radio light curves, which span over 4 orders of magnitude in luminosity, with peak times ranging from a few days to thousands of days (M. F. Bietenholz et al. 2021). This diversity suggests that CCSNe occur with a wide range of CSM densities and spatial distributions. As this is not the case for LFBOTs, we conclude that the CSM properties must be tied to the LFBOT progenitor channel. We discuss the implications of this further in Section 5.2.

We have fewer constraints on the X-ray behavior, as several of the objects only have upper limits on their luminosity (the calculated X-ray luminosity upper limits are driven mostly by their redshift, as Swift determined similar photon count upper limits for each nondetection). But as seen in Figure 4, these upper limits appear to rule out X-ray emission similar to those of jetted TDEs or classical LGRBs while allowing for the possibility of X-ray emission similar to that of AT2018cow. In addition, the order-of-magnitude jump in X-ray luminosity seen in AT2024qfm over just 2 days is much more pronounced than the X-ray variability observed in past LFBOTs.

5.2. Implications for Progenitors

The consistent radio light curves imply consistent properties of the surrounding medium on scales of $\sim 10^{16}$–10^{17} cm. Assuming this medium was produced by material ejected from the progenitor at 1000 km s^{-1}, it probes timescales of a few to tens of years prior to the transient's explosion. Therefore, the radio behavior favors progenitor theories that can explain the presence of a dense ambient medium that is fairly similar from event to event and is produced well in advance of the explosion. This is hard to reconcile with a TDE scenario. R. Margutti et al. (2019) find that the intermediate-mass black holes invoked to explain LFBOTs are unable to sustain outflows sufficient to produce this medium. Difficulties also arise in the massive-star core-collapse model: the stars that we usually suspect to be the progenitors of luminous explosions and energetic SNe are not expected to undergo significant mass loss in such a consistent way just prior to the explosion (indeed, SN radio light curves are highly diverse). On the other hand, progenitor models involving mergers (e.g., B. D. Metzger 2022; D. Tsuna & W. Lu 2025; J. Klencki & B. D. Metzger 2026) naturally explain the dense medium as material ejected from the merger. Each proposed merger scenario involves mass transfer from a massive donor star to a compact object. These papers estimate the circumburst medium density from calculations of the stellar wind from the donor star and mass loss during the merger, and have found them to be consistent with density estimates from past LFBOT papers. These estimates are also expected to hold for each instance of such a merger, explaining the consistency across the LFBOT sample.

5.3. AT2024aehp

AT2024aehp has several characteristics that distinguish it from the other LFBOTs in this paper. Its optical light curve exhibited a plateau at $M = -19$ mag from 5–50 days, behavior we can rule out in AT2023vth and AT2024qfm but not in AT2022abfc, AT2023fhn, and AT2023hkw. AT2024aehp is also an outlier in terms of radio evolution. As shown in Figures 5 and 6, AT2024aehp dramatically brightens in radio luminosity at a later time than the other transients we have discussed, by over an order of magnitude in all frequencies between the $t_{\rm rest} \sim 70$ and 120 day epochs. In contrast, the radio emission of other LFBOTs has already peaked by $t_{\rm rest} \sim 120$ days and begun to shift to lower frequencies. AT2024aehp is also one of only two LFBOTs to have a localization that is consistent with it being a nuclear transient (the other being CSS161010).

The properties of AT2024aehp are reminiscent of TDEs. Most observed TDEs occur in the nucleus as they involve the galaxy's central supermassive black hole (S. Gezari 2021), exhibit late-time radio brightening (A. Horesh et al. 2021; Y. Cendes et al. 2024), and have a slower optical light-curve decay following $t^{-5/3}$ (C. R. Evans & C. S. Kochanek 1989). While known TDEs have optical rises lasting weeks (N. Blagorodnova et al. 2017), a TDE from an intermediate-mass black hole could have a much shorter rise (N. P. M. Kuin et al. 2019; D. A. Perley et al. 2019; C. P. Gutiérrez et al. 2024). Indeed, the transient AT2024puz—which produced luminous optical–UV evolving on an ≈20 day timescale as well as luminous (10^{44} erg s^{-1}) X-ray emission—was posited to be an object intermediate between LFBOTs and TDEs (J. J. Somalwar et al. 2025). Observations of AT2024aehp are ongoing, and a detailed analysis of this transient will be presented in future work.

5.4. Considerations for Future Work

From our work discovering and performing multiwavelength observations of LFBOTs, we have identified areas to improve on for future analysis, summarized below.

Observations. It is unclear how prevalent optical plateaus and late-time radio rebrightenings (as was seen in AT2024aehp) are in LFBOTs. The optical light-curve plateau of AT2024aehp motivates long-term (>10 days) optical monitoring of LFBOTs. As shown in Figure 1, this extended

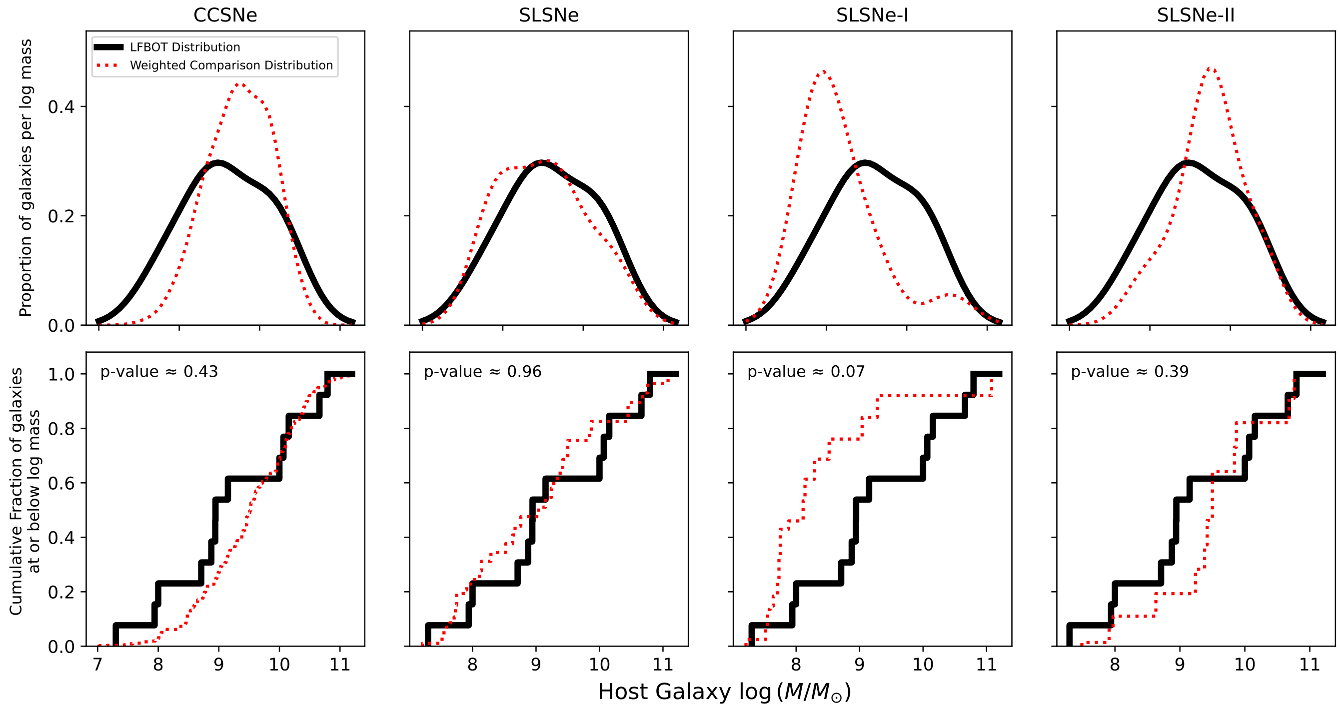

Figure 12. Gaussian KDEs for the LFBOT host-galaxy masses (black) in comparison to the Gaussian KDEs for each of the weighted mass distributions from the K. Taggart & D. A. Perley (2021) CCSN and SLSN host-galaxy populations (dashed red). We also list the p-values from our Kolmogorov–Smirnov (KS) test.

follow-up was not present in our sample's early LFBOTs AT2022abfc, AT2023fhn, and AT2023hkw, which limits our ability to constrain the presence of a similar plateau. In addition, late-time radio follow-up observations should be obtained to search for rebrightenings on timescales of hundreds of days.

Another gap in our follow-up observations is the lack of X-ray detections for most of these LFBOTs. Swift observations were not sensitive enough to rule out levels of X-ray emission that have already been detected in previous LFBOTs such as CSS161010 (D. L. Coppejans et al. 2020) and AT2018cow (D. A. Perley et al. 2019). Going forward, deeper Chandra observations should be obtained for each object, as was done in, e.g., AT2023fhn (A. A. Chrimes et al. 2024a). X-ray detections will let us verify that the X-ray emission is in excess of the extrapolated synchrotron SED, confirming that it originates from a different source, like in previous LFBOTs (e.g., R. Margutti et al. 2019; J. S. Bright et al. 2022). This also allows us to track the ratio of X-ray to UV–optical flux over time. Under the proposed scenario that the UV–optical flux is reprocessed high-energy radiation (R. Margutti et al. 2019; N. LeBaron et al. 2026), this would enable us to track the optical depth of the ejecta's reprocessing layer. Finally, as the X-ray flux is thought to originate from a central object (A. Y. Q. Ho et al. 2019; B. D. Metzger 2022; A. J. Nayana et al. 2025), it is one of the few probes of the regions closest to the transient's center.

Modeling. The models we use in this paper's analysis could be improved upon or have assumptions that could be relaxed to explore a wider range of parameter space.

We use the model of R. A. Chevalier (1998) to derive properties of the shock and ambient medium from our radio and millimeter observations. This formulation requires assuming that certain conditions hold, such as the equipartition of energy, a nonthermal electron energy distribution, and that the shock is spherical and nonrelativistic. The nonrelativistic assumption will introduce some inaccuracies, as we calculate some values of $\Gamma\beta$ that are greater than 0.5. We also assume values for the filling factor f, ϵ_e, ϵ_B, and the electron power-law index, and our results do depend on these parameters. A future analysis could relax some of these assumptions or fit for parameters that we set to be fixed. Some of these flaws can be inferred from our fitting results. According to R. A. Chevalier (1998), the broken power-law fit should have a $\nu^{5/2}$ dependence in the optically thick regime and a $\nu^{-(p-1)/2}$ dependence in the optically thin regime, where p is the electron power-law index. We assume $p = 3$, so the optically thin dependence should be as ν^{-1}. However, for most epochs we do not have enough detections to confirm a $\nu^{5/2}$ dependence in the optically thick regime (Figure 6). In addition, from the results shown in Table 7, the observed slopes in the optically thin regime are not all consistent with ν^{-1}. Work has already been done to extend this model to account for thermal electrons (B. Margalit & E. Quataert 2021) and relativistic effects (B. Margalit & E. Quataert 2024; R. Ferguson & B. Margalit 2026). Generalizing and refining the synchrotron model would help obtain more rigorous estimates of shock and ambient medium parameters. For example, relativistic effects become significant at $\Gamma\beta \gtrsim 1$—which some of our LFBOTs approach—where results can differ by an order of magnitude (R. Ferguson & B. Margalit 2026). Our conclusions would still be applicable as they rely on the similarity of the radio emission between LFBOTs, but our numerical results can be significantly affected. As our paper's scope is to present new observational data for six LFBOTs and use techniques analogous to those in previous LFBOTs papers to compare properties across this sample, we defer the application of improved synchrotron radiation models to future work.

In our `prospector` fits for the LFBOT host-galaxy properties, we used a single prescription for the SFH, dust model, and initial mass function, but a future analysis should ensure that results are robust to different choices for these parameters. In particular, we use a parametric SFH to match the work of previous LFBOT papers, but internal testing with a nonparametric SFH produced results that differ by about 1σ. We also omit the spectra when performing our fits, as it is difficult to standardize spectra from different observing conditions, processed through different software, and possessing different levels of contamination from the transient itself. This required us to use the mass–metallicity relation in A. Gallazzi et al. (2005) to fix a metallicity in our models. As the mass is largely set by the galaxy's overall luminosity, we expect that this would lead to little change in our mass estimates, but will bias our metallicity estimates to more moderate values. We have also observed that the SFR estimate is insensitive to changes in metallicity. So, our method does introduce a caveat to our metallicity estimates, but we still have confidence in our host-galaxy analysis as it relies on the mass and SFR. Still, incorporating a host-galaxy spectrum obtained after the transient faded would produce a more accurate result. After the submission of this paper, A. E. Nugent et al. (2026) performed a `prospector` LFBOT host-galaxy analysis with a nonparametric SFH and utilized host-galaxy spectroscopy when available. They find similar results for the hosts of AT2023fhn and AT2024qfm, but have larger host-galaxy masses by a factor of a few for AT2023hkw and AT2023vth.

Selection bias. Our requirements for LFBOT classification introduce biases that are difficult to account for. For example, the requirement of a visible host galaxy biases our sample toward more luminous hosts. While we did account for some bias in our LFBOT sample in our study on host-galaxy masses, we caution that we did not perform any such correction for our analysis of host-galaxy offsets. Another source of bias is our requirement of an X-ray and radio detection. While this would exclude LFBOTs that are X-ray and radio faint, our procedure's success rate of detecting X-rays or radio emission from promising LFBOT candidates implies that the loss is not significant. Finally, all of these LFBOTs were selected on the basis of their optical light curves. As we discussed in Section 5.1, this would bias our LFBOTs to have similar optical light-curve properties, such as their absolute luminosities and rise and decay rates. This could lead us to miss any diversity in LFBOT optical characteristics (e.g., J. J. Somalwar et al. 2025).

Future surveys. The development of the Vera C. Rubin Observatory (Rubin) (Ž. Ivezić et al. 2019) and its deep, wide-field optical imaging survey is expected to increase the transient discovery rate by orders of magnitude. This would cause the number of known LFBOTs to increase significantly, paving the way for more robust analysis. The results presented in this paper inform how to best handle each new LFBOT discovery and serve as a blueprint for statistical analysis of an expanded LFBOT sample.

Rubin data, along with the advent of high-cadence wide-field UV surveys such as the Ultraviolet Transient Astronomy Satellite (ULTRASAT; Y. Shvartzvald et al. 2024) and the Ultraviolet Explorer (UVEX; S. R. Kulkarni et al. 2021), will enable LFBOTs to be identified and followed up much earlier in their evolution. Rubin's sensitivity can allow for detections before the optical peak, allowing us to identify rapid rising light curves within a couple of days. Photometric classifiers can potentially screen out LFBOT false positives, mitigating the dependence on the presence of a host galaxy for classification. Meanwhile, ULTRASAT's rapid cadence (5 minutes) means that an LFBOT's fast brightening can be identified in a matter of hours. Faster discoveries enable earlier radio observations at $t_{\rm obs} \leqslant 5$ days, probing smaller shock radii and more recent mass-loss history. Early UV observations, in conjunction with near-IR observations, can show evidence of a dust echo, providing an independent measure of the surrounding CSM (B. D. Metzger & D. A. Perley 2023). The UV can also provide better estimates of the early photospheric radius and effective temperatures, as fits to only optical detections can be uncertain (M. Pursiainen et al. 2025). Additionally, time-domain surveys outside the optical band can provide a new avenue to find LFBOTs. These surveys may show that LFBOTs are part of a more diverse sample that we have only begun to study. In all, the ability to detect and study LFBOTs over a broader suite of observatories and surveys can remedy some of the challenges of our current studies.

6. Summary

We presented multiwavelength data—including optical photometry, optical spectroscopy, Swift X-ray observations, and VLA, NOEMA, and uGMRT radio observations—of six LFBOTs (AT2022abfc, AT2023fhn, AT2023hkw, AT2023vth, AT2024qfm, and AT2024aehp) at redshifts spanning $z = 0.0747$–0.339. We identified all of these objects on the basis of fast light-curve evolution in ZTF survey data, and confirmed their similarity to the prototype AT2018cow via radio detections. Five of the six LFBOTs (all except AT2023fhn) are presented here for the first time. Our work increases the known number of LFBOTs by 50%.

The optical light curves of four of these events fade by 3–4 mag over $t_{\rm rest} \approx 10$ days, similarly to AT2018cow. A fifth event, AT2022abfc, did not have deep photometric follow-up to confirm fading over this timescale, but had a similar decay rate over the first 5 days. The last, AT2024aehp, exhibited a plateau at $M \approx -19$ mag over tens of days, after an initial fast decline. The optical spectra do not show any clear features from the transients themselves, including a spectrum of AT2024aehp during its plateau phase.

The X-ray luminosity of AT2024qfm is among the highest of all LFBOTs to date, at 10^{44} erg s^{-1} at $t_{\rm rest} \approx 1$ week. The X-rays also appeared to show a brightening by an order of magnitude over just a few days. Swift X-ray observations of the other objects resulted in nondetections that were not deep enough to rule out emission identical to AT2018cow itself. AT2023fhn was detected by Chandra at similar levels to AT2018cow (A. A. Chrimes et al. 2024b; A. J. Nayana et al. 2025).

The 10 GHz radio light curves peak at $t_{\rm rest} \approx 50$–100 days, with peak luminosities primarily in the range of 10^{39}–10^{40} erg s^{-1}. During the rise, the emission appears to be self-absorbed, confirmed by multiband VLA observations, as well as by NOEMA 100 GHz detections for AT2024qfm and AT2023vth. We measured basic shock parameters using a simple equipartition analysis, and found—as for previous LFBOTs—fast but subrelativistic shock speeds. The exception to the radio behavior is AT2024aehp, which, starting at $t_{\rm rest} \approx 70$ days, displayed rapid brightening. This late-time brightening is reminiscent of TDEs. Observations of

AT2024aehp are ongoing, and will be presented in future work.

For all objects, we measured the offset of the transient position from the host-galaxy nucleus, as well as the basic host-galaxy properties (e.g., stellar mass or SFR). Combining our results with all literature objects, for a total sample of 13 objects, we find that the offset distribution appears intermediate to CCSNe and SLSNe. We find that the host-galaxy masses and SFRs trace the full CCSN sequence, and that—even correcting for the fact that we are biased toward detecting LFBOTs in higher-mass galaxies, due to our requirement of a host-galaxy detection—the intrinsic mass distribution appears to be consistent with both SLSNe and CCSNe.

The similar radio light curves imply a similar circumburst medium for LFBOTs, and therefore a progenitor scenario that can produce a consistent medium timed with the terminal event, such as the merger of a massive star with a compact object. This argument was made when the sample size of LFBOTs was much smaller (B. D. Metzger 2022), but here we confirm it with a much larger number of events. For future LFBOT studies, we would suggest longer-term optical monitoring (to confirm or rule out the presence of a plateau as observed in AT2024aehp), deeper X-ray observations (i.e., with Chandra), and selection in other bands of the electromagnetic spectrum to mitigate some of the biases present here. LFBOT studies are also poised to benefit from new and upcoming surveys. The deep sensitivity of the Legacy Survey of Space and Time on Rubin and the development of very-high-cadence surveys like ULTRASAT can simultaneously expand our number of LFBOTs and enable us to study them in greater depth. These observatories, among others such as UVEX and the Argus Array, can provide breakthroughs in our understanding of LFBOTs.

Acknowledgments

We thank the reviewer and the journal editors for their insightful and constructive feedback.

We thank Dusán Tubín for assistance using the eROSITA upper limit service; Ryan Chornock for providing a AT2024qfm LRIS spectrum; and Raffaella Margutti and Joe Bright for useful discussions.

This work was performed in part at the Aspen Center for Physics, which is supported by National Science Foundation grant PHY-2210452.

A.Y.Q.H., C.S., M.C., and G.S. acknowledge support from a Sloan Research Fellowship (Award Number FG-2024-21320) from the Alfred P. Sloan Foundation, a Packard Fellowship from the David and Lucile Packard Foundation, National Aeronautics and Space Administration (NASA) grant 80NSSC24K0377, an LSST Scialog Early Science grant from the Research Corporation for Science Advancement, and Hubble Space Telescope (HST) grant HST-GO-17477.006-A.

M.W.C. acknowledges support from the U.S. National Science Foundation (NSF) with grant numbers PHY-2409481, PHY-2308862, and PHY-2117997. A.V.F.'s group at UC Berkeley received financial assistance from the Christopher R. Redlich Fund, as well as donations from Gary and Cynthia Bengier, Clark and Sharon Winslow, Alan Eustace and Kathy Kwan, William Draper, Timothy and Melissa Draper, Briggs and Kathleen Wood, Sanford Robertson (W.Z. is a Bengier-Winslow-Eustace Specialist in Astronomy, T.G.B. is a Draper-Wood-Robertson Specialist in Astronomy, and Y.Y. was a Bengier-Winslow-Robertson Fellow in Astronomy), and numerous other donors. A.G.Y.'s research is supported by ISF, IMOS, and BSF grants, as well as the André Deloro Institute for Space and Optics Research, the Center for Experimental Physics, a WIS-MIT Sagol grant, the Norman E Alexander Family M Foundation ULTRASAT Data Center Fund, and Yeda-Sela; A.G.Y. is the incumbent of the The Arlyn Imberman Professorial Chair. C.L. is supported by DoE award #DE-SC0025599. B.M. is supported in part by the National Science Foundation under grant number AST-2508620. N.R. is supported by a Northwestern University Presidential Fellowship Award. Zwicky Transient Facility and MMT Observatory access for N.R. was supported by Northwestern University and the Center for Interdisciplinary Exploration and Research in Astrophysics (CIERA). This work is supported by the U.S. NSF under Cooperative Agreement PHY-2019786 (The NSF AI Institute for Artificial Intelligence and Fundamental Interactions).[49]

We thank the staff of the various observatories at which data were obtained.

Based in part on observations obtained with the Samuel Oschin Telescope 48 inch (P48) and the 60 inch Telescope at the Palomar Observatory as part of the Zwicky Transient Facility project. ZTF is supported by the National Science Foundation under Grant Nos. AST-1440341, AST-2034437, and currently Award #2407588. ZTF receives additional funding from the ZTF partnership. Current members include Caltech, USA; Caltech/IPAC, USA; University of Maryland, USA; University of California, Berkeley, USA; University of Wisconsin at Milwaukee, USA; Cornell University, USA; Drexel University, USA; University of North Carolina at Chapel Hill, USA; Institute of Science and Technology, Austria; National Central University, Taiwan; and OKC, University of Stockholm, Sweden. Operations are conducted by Caltech's Optical Observatory (COO), Caltech/IPAC, and the University of Washington at Seattle, USA.

SED Machine is based upon work supported by the National Science Foundation under Grant No. 1106171.

Some of the data presented herein were obtained at W. M. Keck Observatory, which is a private 501(c)3 nonprofit organization operated as a scientific partnership among the California Institute of Technology, the University of California, and NASA. The Observatory was made possible by the generous financial support of the W. M. Keck Foundation. This research has made use of the Keck Observatory Archive (KOA), which is operated by the W. M. Keck Observatory and the NASA Exoplanet Science Institute (NExScI), under contract with NASA. This work was enabled by observations made from the Gemini North telescope, located within the Maunakea Science Reserve and adjacent to the summit of Maunakea. We are grateful for the privilege of observing the Universe from a place that is unique in both its astronomical quality and its cultural significance. The authors wish to recognize and acknowledge the very significant cultural role and reverence that the summit of Maunakea has always had within the indigenous Hawaiian community. We are most fortunate to have the opportunity to conduct observations from this mountain.

This research has made use of the NASA/IPAC Extragalactic Database (NED), which is funded by NASA and operated by the California Institute of Technology, as well as data and software provided by the High Energy Astrophysics

[49] http://iaifi.org/

Science Archive Research Center (HEASARC), which is a service of the Astrophysics Science Division at NASA/GSFC.

The Liverpool Telescope is operated on the island of La Palma by Liverpool John Moores University in the Spanish Observatorio del Roque de los Muchachos of the Instituto de Astrofisica de Canarias with financial support from the UK Science and Technology Facilities Council.

Observations reported here were obtained in part at the MMT Observatory, a joint facility of the Smithsonian Institution and the University of Arizona. Based in part on observations made with the Nordic Optical Telescope, owned in collaboration by the University of Turku and Aarhus University, and operated jointly by Aarhus University, the University of Turku and the University of Oslo, representing Denmark, Finland, and Norway, the University of Iceland and Stockholm University at the Observatorio del Roque de los Muchachos, La Palma, Spain, of the Instituto de Astrofisica de Canarias. The NOT data were obtained under program ID P68-501.

These results made use of the Lowell Discovery Telescope (LDT) at Lowell Observatory. Lowell is a private, nonprofit institution dedicated to astrophysical research and public appreciation of astronomy and operates the LDT in partnership with Boston University, the University of Maryland, the University of Toledo, Northern Arizona University, and Yale University. The Large Monolithic Imager was built by Lowell Observatory using funds provided by the U.S. NSF (AST-1005313). This paper includes data gathered with the 6.5 m Magellan Telescopes located at Las Campanas Observatory, Chile. Based in part on observations obtained at the Southern Astrophysical Research (SOAR) telescope, which is a joint project of the Ministério da Ciência, Tecnologia e Inovações (MCTI/LNA) do Brasil, the U.S. NSF's NOIRLab, the University of North Carolina at Chapel Hill (UNC), and Michigan State University (MSU).

Based in part on observations processed using Data Reduction for Astronomy from Gemini Observatory North and South (DRAGONS), obtained at the international Gemini Observatory, program of NSF NOIRLab, which is managed by the Association of Universities for Research in Astronomy (AURA) under a cooperative agreement with the U.S. NSF on behalf of the Gemini Observatory partnership: the U.S. NSF (United States), National Research Council (Canada), Agencia Nacional de Investigación y Desarrollo (Chile), Ministerio de Ciencia, Tecnología e Innovación (Argentina), Ministério da Ciência, Tecnologia, Inovações e Comunicações (Brazil), and Korea Astronomy and Space Science Institute (Republic of Korea).

The National Radio Astronomy Observatory is a facility of the U.S. NSF operated under cooperative agreement by Associated Universities, Inc. This work is based on observations carried out under project numbers D24AA, W22BT, and S23BF with the IRAM NOEMA Interferometer. IRAM is supported by INSU/CNRS (France), MPG (Germany), and IGN (Spain). GMRT is run by the National Centre for Radio Astrophysics of the Tata Institute of Fundamental Research.

We acknowledge the use of public data from the Swift data archive. This research is based on observations made with the Galaxy Evolution Explorer and the Neil Gehrels Swift Observatory, obtained from the MAST data archive at the Space Telescope Science Institute, which is operated by the Association of Universities for Research in Astronomy, Inc., under NASA contract NAS 5-26555.

The Pan-STARRS1 Surveys (PS1) and the PS1 public science archive have been made possible through contributions by the Institute for Astronomy, the University of Hawaii, the Pan-STARRS Project Office, the Max-Planck Society and its participating institutes, the Max Planck Institute for Astronomy, Heidelberg and the Max Planck Institute for Extraterrestrial Physics, Garching, The Johns Hopkins University, Durham University, the University of Edinburgh, the Queen's University Belfast, the Harvard-Smithsonian Center for Astrophysics, the Las Cumbres Observatory Global Telescope Network Incorporated, the National Central University of Taiwan, the Space Telescope Science Institute, NASA under grant #NNX08AR22G issued through the Planetary Science Division of the NASA Science Mission Directorate, NSF grant AST-1238877, the University of Maryland, Eotvos Lorand University (ELTE), the Los Alamos National Laboratory, and the Gordon and Betty Moore Foundation.

The Legacy Surveys consist of three individual and complementary projects: the Dark Energy Camera Legacy Survey (DECaLS; Proposal ID #2014B-0404; PIs: D. Schlegel and A. Dey), the Beijing-Arizona Sky Survey (BASS; NOAO Prop. ID #2015A-0801; PIs: Zhou Xu and Xiaohui Fan), and the Mayall z-band Legacy Survey (MzLS; Prop. ID #2016A-0453; PI: A. Dey). DECaLS, BASS, and MzLS together include data obtained, respectively, at the Blanco telescope, Cerro Tololo Inter-American Observatory, NSF's NOIRLab; the Bok telescope, Steward Observatory, University of Arizona; and the Mayall telescope, Kitt Peak National Observatory, NOIRLab. Pipeline processing and analyses of the data were supported by NOIRLab and the Lawrence Berkeley National Laboratory (LBNL). The Legacy Surveys project is honored to be permitted to conduct astronomical research on Iolkam Du'ag (Kitt Peak), a mountain with particular significance to the Tohono O'odham Nation.

NOIRLab is operated by the Association of Universities for Research in Astronomy (AURA) under a cooperative agreement with the U.S. LBNL is managed by the Regents of the University of California under contract to the U.S. Department of Energy.

This project used data obtained with the Dark Energy Camera (DECam), which was constructed by the Dark Energy Survey (DES) collaboration. Funding for the DES Projects has been provided by the U.S. Department of Energy, the U.S. NSF, the Ministry of Science and Education of Spain, the Science and Technology Facilities Council of the United Kingdom, the Higher Education Funding Council for England, the National Center for Supercomputing Applications at the University of Illinois at Urbana-Champaign, the Kavli Institute of Cosmological Physics at the University of Chicago, Center for Cosmology and Astro-Particle Physics at the Ohio State University, the Mitchell Institute for Fundamental Physics and Astronomy at Texas A&M University, Financiadora de Estudos e Projetos, Fundacao Carlos Chagas Filho de Amparo, Financiadora de Estudos e Projetos, Fundacao Carlos Chagas Filho de Amparo a Pesquisa do Estado do Rio de Janeiro, Conselho Nacional de Desenvolvimento Cientifico e Tecnologico and the Ministerio da Ciencia, Tecnologia e Inovacao, the Deutsche Forschungsgemeinschaft and the Collaborating Institutions in the Dark Energy Survey. The Collaborating

Institutions are Argonne National Laboratory, the University of California at Santa Cruz, the University of Cambridge, Centro de Investigaciones Energeticas, Medioambientales y Tecnologicas-Madrid, the University of Chicago, University College London, the DES-Brazil Consortium, the University of Edinburgh, the Eidgenossische Technische Hochschule (ETH) Zurich, Fermi National Accelerator Laboratory, the University of Illinois at Urbana-Champaign, the Institut de Ciencies de l'Espai (IEEC/CSIC), the Institut de Fisica d'Altes Energies, Lawrence Berkeley National Laboratory, the Ludwig Maximilians Universitat Munchen and the associated Excellence Cluster Universe, the University of Michigan, NSF's NOIRLab, the University of Nottingham, the Ohio State University, the University of Pennsylvania, the University of Portsmouth, SLAC National Accelerator Laboratory, Stanford University, the University of Sussex, and Texas A&M University.

BASS is a key project of the Telescope Access Program (TAP), which has been funded by the National Astronomical Observatories of China, the Chinese Academy of Sciences (the Strategic Priority Research Program "The Emergence of Cosmological Structures" grant #XDB09000000), and the Special Fund for Astronomy from the Ministry of Finance. The BASS is also supported by the External Cooperation Program of Chinese Academy of Sciences (grant #114A11KYSB20160057), and Chinese National Natural Science Foundation (grants #12120101003 and #11433005).

The Legacy Surveys imaging of the DESI footprint is supported by the Director, Office of Science, Office of High Energy Physics of the U.S. Department of Energy under Contract No. DE-AC02-05CH1123, by the National Energy Research Scientific Computing Center, a DOE Office of Science User Facility under the same contract, and by the U.S. NSF, Division of Astronomical Sciences under Contract No. AST-0950945 to NOAO.

This publication makes use of data products from the Near-Earth Object Wide-field Infrared Survey Explorer (NEOWISE), which is a joint project of the Jet Propulsion Laboratory–California Institute of Technology and the University of California, Los Angeles. NEOWISE is funded by NASA.

This work is based on data from eROSITA, the soft X-ray instrument aboard SRG, a joint Russian-German science mission supported by the Russian Space Agency (Roskosmos), in the interests of the Russian Academy of Sciences represented by its Space Research Institute (IKI), and the Deutsches Zentrum für Luft- und Raumfahrt (DLR). The SRG spacecraft was built by Lavochkin Association (NPOL) and its subcontractors, and is operated by NPOL with support from the Max Planck Institute for Extraterrestrial Physics (MPE). The development and construction of the eROSITA X-ray instrument was led by MPE, with contributions from the Dr. Karl Remeis Observatory Bamberg & ECAP (FAU Erlangen-Nuernberg), the University of Hamburg Observatory, the Leibniz Institute for Astrophysics Potsdam (AIP), and the Institute for Astronomy and Astrophysics of the University of Tübingen, with the support of DLR and the Max Planck Society. The Argelander Institute for Astronomy of the University of Bonn and the Ludwig Maximilians Universität Munich also participated in the science preparation for eROSITA.

Data Availability

All data and code underlying this paper are available at https://github.com/CassieSev/Multiwavelength-Analysis-of-Six-LFBOTs and at Zenodo at DOI: 10.5281/zenodo.20819447.

Facilities: Blanco (DECaLS), Bok (BASS), DCT (LMI), GALEX, Gemini:Gillett, Gemini:South, GMRT, IRAM: NOEMA, Keck:I (LRIS), Keck:II (KCWI DEIMOS), Liverpool:2m, Magellan:Baade (IMACS), Mayall (MzLS), MMT (Binospec), NOT (ALFOSC), PO:1.2m, PO:1.5m, Sloan, SOAR (GHTS), Swift, VLA, NEOWISE.

Appendix A
Identification and Classification

In this section, we describe how each LFBOT was identified in the ZTF alert stream, and describe the initial follow-up observations that led to their classification as an LFBOT. ZTF observations of the six LFBOTs in this paper occurred during Phase II (ZTF-II), which was divided into public (50%), partnership (30%), and Caltech (20%) observing time. ZTF uses three filters: *ztf-g*, *ztf-r*, and *ztf-i*. For comparison with other photometry, we denote these as g, r, and i, respectively. ZTF data products are processed by the IPAC ZTF pipeline (F. J. Masci et al. 2019), which uses image subtraction following the methods of B. Zackay et al. (2016). Detections more significant that 5σ are distributed as alerts in the Avro format (M. T. Patterson et al. 2019). These alerts are filtered using machine learning real–bogus metrics (A. Mahabal et al. 2019; D. A. Duev et al. 2019), host-galaxy classifiers (Y. Tachibana & A. A. Miller 2018), and inspection of light-curve properties. For ZTF-II, the collaboration used the Fritz marshal (S. van der Walt et al. 2019; D. A. Duev et al. 2019) to coordinate detection, analysis, and follow-up observations of transients. The Fritz marshal uses the open-source software package `SkyPortal` (M. W. Coughlin et al. 2023).

A.1. AT2022abfc/ZTF22abvrxkk

AT2022abfc was first detected by ZTF on 2022 November 21 (MJD 59904.344; C. Fremling 2022). ZTF nondetections prior to the first observation and ZTF detections over the next 5 days confirmed a rise faster than 1 mag day^{-1} and a decay rate of 0.2 mag day^{-1}. The transient's fast evolution led to follow-up multiwavelength observations. A Gemini South spectrum taken 2022 December 1 showed narrow Hα emission and Ca II H and K absorption lines at $z = 0.212$, implying a peak absolute magnitude of -20.7 (A. Y. Q. Ho et al. 2022a). A radio follow-up campaign with the VLA began with a detection at 10 GHz on December 6 (A. Y. Q. Ho et al. 2022a). Subsequent radio observations showed a brightening of the radio emission. The transient's fast evolution, high luminosity, and radio emission led to its classification as an LFBOT.

A.2. AT2023fhn/ZTF23aaeozpp/ATLAS23hnk

The discovery narrative for AT2023fhn has already been published by A. A. Chrimes et al. (2024b); we reiterate it here for convenience. ZTF first detected AT2023fhn on 2023 April 10 (MJD 60044.204; C. Fremling 2023a). The source was also detected by ATLAS (J. L. Tonry et al. 2018), 1 day later. Its light curve showed a fast decay of 0.2 mag day^{-1} and blue optical colors ($g - r \approx -0.5$ mag). A possible host galaxy's photometric redshift implied an absolute optical magnitude of

$M_g < -20$, motivating follow-up observations. On April 20, a spectrum obtained by the DBSP on the Palomar 5 m telescope yielded Hα, N II, and S II emission lines at $z = 0.24$, confirming an absolute magnitude of $M_g = -21.5$ (A. Y. Q. Ho et al. 2023a). The transient was subsequently detected at X-ray and radio wavelengths, respectively, by Chandra on April 25 (A. Chrimes et al. 2023) and the VLA (10 GHz) on June 15 (A. Y. Q. Ho 2023a). The blue colors, fast fading, high luminosity, and detected emission throughout the electromagnetic spectrum confirmed it as an LFBOT. The Chandra X-ray detections and a subset of this transient's VLA radio observations are already published by A. A. Chrimes et al. (2024a).

A.3. AT2023hkw/ZTF23aaimsja

ZTF first detected AT2023hkw on 2023 May 1 (MJD 60065.199; C. Fremling 2023b). The transient was flagged for fast evolution from a rise rate greater than 1 mag day^{-1} and a decay rate of ∼0.2 mag day^{-1}. This resulted in follow-up spectroscopy on May 12 using DEIMOS at the Keck Observatory (M. L. Li et al. 2023), using 1440 s of exposure time. The spectrum showed narrow Hα and [N II] emission lines from the host galaxy at $z = 0.339$, implying an absolute magnitude of $M_g = -21$. It was also detected by the VLA at 10 GHz on June 14 (A. Y. Q. Ho 2023b). It was classified as an LFBOT from its luminosity, fast evolution, and radio emission.

A.4. AT2023vth/ZTF23ableqsp

ZTF first detected AT2023vth on 2023 October 18 (MJD 60235.116; C. Fremling 2023c). It had a fast rise of 1 mag day^{-1}, a fast fade of 0.25 mag day^{-1}, and blue colors with $g - r \approx -0.4$ mag (J. Sevilla et al. 2023), making it a promising LFBOT candidate. Optical spectroscopy taken on November 12 revealed narrow Hα, [N II], and [S II] emission lines from the host galaxy at $z = 0.0747$, which implied an absolute magnitude of $M_g \approx -20$ (A. Y. Q. Ho et al. 2023a). The VLA detected radio emission at 10 GHz on November 17 (A. Y. Q. Ho 2023c) and NOEMA found millimeter emission at 100 GHz on November 20 (A. Y. Q. Ho & M. Bremer 2023). The presence of multiwavelength emission solidified the transient's LFBOT classification. We also obtained deep late-time VLT observations that will be reported in a separate paper according to a prior arrangement (J. L. Wise et al. 2026, in preparation).

A.5. AT2024qfm/ZTF24aaxhxhf

AT2024qfm was first detected by ZTF on 2024 July 24 (MJD 60515.41; F. Forster et al. 2024). The most recent nondetection was 0.98 days prior at $g > 19.27$ mag. The source was detected again three nights later as part of the ZTF public survey, resulting in the first alert. Over the following two nights the source exhibited significant fading of 0.3 mag day^{-1}. Sloan Digital Sky Survey (SDSS) preimaging showed a galaxy at the transient's position with photometric redshift $z = 0.190 \pm 0.054$, implying a high luminosity of $M < -20$ mag. The rapid fading, host-galaxy counterpart, and high luminosity led the transient to be flagged by the daily scanner on July 27.

The rapid fading flagged several fast-transient pipelines including Fastfinder (M. Fulton et al. 2024) and ZTFReST (I. Andreoni et al. 2021). The rapid fading was publicly reported by Fastfinder (M. Fulton et al. 2024). The transient itself was reported to the Transient Name Server (TNS)[50] by the Automatic Learning for the Rapid Classification of Events (ALeRCE) broker (F. Forster et al. 2024).

On August 1, a redshift of $z = 0.2270$ was determined by J. H. Gillanders et al. (2024) and an X-ray detection was reported by R. Margutti et al. (2024). On August 2, we obtained a long-slit spectrum of AT2024qfm with GMOS on Gemini North under a ToO program[51] and confirmed the reported redshift. A VLA radio observation was also obtained (A. Y. Q. Ho 2024); the radio data will be published as part of a separate paper (A. J. Nayana et al. 2026, in preparation). Finally, we obtained 100 GHz observations using NOEMA, which resulted in a detection. The fast optical light curve and high luminosities at millimeter and X-ray wavelengths all confirmed the LFBOT nature of this source. We also obtained deep late-time Gran Telescopio Canarias HiPERCAM observations that will be reported in a separate paper (J. L. Wise et al. 2026, in preparation).

A.6. AT2024aehp/ZTF24abygbss

AT2024aehp was first detected by ZTF on 2024 December 19 (MJD 60663.36) and reported to the TNS by ALeRCE (A. Munoz-Arancibia et al. 2024). The most recent nondetection was 3 days prior. ZTF photometry over the next two nights revealed a decay rate of 0.2 mag day^{-1}, causing the transient to be flagged by the daily scanner on December 21. The fast fading, blue colors ($g - r \approx -0.3$ mag) and possible high peak luminosity from the photometric redshift of the host galaxy (SDSS $z_{\rm ph} = 0.17 \pm 0.09$) motivated us to trigger follow-up observations. We acquired spectroscopy of the candidate using GMOS on Gemini South on 2024 December 23. The spectrum shows narrow Hα, [N II], and [S II] emission lines that correspond to $z = 0.170$. We reported the rapid evolution and the high luminosity inferred from the spectroscopy. (J. Sevilla et al. 2024).

Radio and X-ray observations initially resulted in nondetections, and the optical light curve flattened out in a way uncharacteristic of LFBOTs (G. Schroeder et al. 2025). A subsequent radio epoch at 86 days after peak light resulted in a detection and confirmation of a positive spectral index, suggesting a link with AT2018cow-like LFBOTs (G. Schroeder & A. Y. Q. Ho 2025). Then, another epoch at 141 days showed brightening in all radio bands by almost an order of magnitude, which is unprecedented compared to the radio emission of other LFBOTs. This paper focuses on the early observations of AT2024aehp, and the interesting late-time behavior will be examined in separate work.

Appendix B
Data Tables

In this section we provide tables of optical spectroscopy (Table 2), X-ray observations (Table 3), radio observations (Table 4), and host-galaxy photometry (Table 5). We display the result of our prospector fits in Table 6. We also give our broken power-law fits to the radio SEDs (Table 7) and the resulting synchrotron parameters (Table 8). Finally, we list the optical photometry for each transient in Table 9.

[50] https://www.wis-tns.org/

[51] GN-2024B-Q-128; PI: A. Ho.

Table 2
Optical Spectroscopy

Object	UTC Date (YYYYMMDD)	$t_{\rm obs}$ (days)	Telescope/Inst.	Exposures (s)	PI and Program	Reduction Software
AT2022abfc	20221201	10	Gemini-S/GMOS	6 × 450	GS-2022B-Q-126; PI: A. Ho	`DRAGONS`[a]
AT2023fhn	20230419	7	Gemini-S/GMOS	6 × 450	GS-2023A-Q-127; PI: A. Ho	`DRAGONS`[a]
AT2023fhn	20230420	8	P200/DBSP	3 × 600	PI: Y. Qin	`DBSP_DRP`[b]
AT2023fhn	20230426	14	Keck I/LRIS	4 × 2700	PI: M. M. Kasliwal	`lpipe`[c]
AT2023hkw	20230512	12	Keck II/DEIMOS	1440	PI: A. Filippenko	IRAF routines and custom codes [d]
AT2023vth	20231022	2	P200/SEDM	∼1800[e]	…[e]	…[e]
AT2023vth	20231112	23	Gemini-N/GMOS	2 × 500	GN-2023B-Q-130; PI: A. Chrimes	`DRAGONS`[a]
AT2024qfm	20240802	6	Gemini-N/GMOS	4 × 450	GN-2024B-Q-128; PI: A. Ho	`DRAGONS`[a]
AT2024qfm	20240809	13	Keck I/LRIS	4 × 875	U256; PI: Chornock	`lpipe`[c]
AT2024qfm	20240831	35	MMT/Binospec	1200	UAO-G200-24B; PI: A. A. Miller	Binospec and `pypeit`[f]
AT2024qfm	20240902	37	Keck I/LRIS	4 × 900	U233; PI: Filippenko	`lpipe`[c]
AT2024aehp	20241224	5	Gemini-S/GMOS	4 × 450	GS-2024B-Q-121 ; PI: A. Ho	`DRAGONS`[a]
AT2024aehp	20250101	13	Keck II/KCWI	600 + 3 × 180	PI: Y. Qin	`kskywizard`[g]
AT2024aehp	20250107	19	MMT/Binospec	4 × 500	PI: A. Gal-Yam	Binospec and `pypeit`[f]

Notes.
[a] `DRAGONS` (K. Labrie et al. 2023) is a software package specialized for reducing Gemini data, and performs stacking of flat fields and comparison lamps, bias subtraction, and standard-star flux calibration.
[b] `DBSP_DRP` (M. S. Mandigo-Stoba et al. 2022) is a Python package based on `pypeit` (J. X. Prochaska et al. 2020) that performs automated reduction of DBSP data, including atmospheric corrections and flux calibration.
[c] `lpipe` (D. A. Perley 2019) is an IDL pipeline that performs for fully automated data reduction for the LRIS instrument. Its steps include bias correction, flat-fielding, and wavelength and flux calibration.
[d] The IRAF routines (J. M. Silverman et al. 2012; D. Tody 1986; https://iraf-community.github.io) routines and custom Python and IDL codes (https://iraf-community.github.io) use techniques for CCD processing and spectrum extraction, comparison-lamp wavelength calibration, and standard-star flux calibration.
[e] This spectrum was taken as part of automated follow-up for the ZTF Bright Transient Survey (C. Fremling et al. 2020).
[f] A Binospec pipeline (J. Kansky et al. 2019) was used to perform bias subtraction and flat-fielding, while `pypeit` (J. X. Prochaska et al. 2020) was used to perform cosmic-ray removal, wavelength calibration, and relative-flux calibration from a standard star.
[g] `kskywizard` (https://iraf-community.github.io) is a pipeline that can perform sky subtraction, flux calibration, and telluric correction.

Table 3
Swift XRT Observations

Object	UTC Date (YYYYMMDD)	$t_{\rm obs}$ (days)	Flux (10^{-13} erg cm^{-2} s^{-1})	Count Rate (10^{-3} s^{-1})	$n_{\rm H}$ (10^{20} cm^{-2})	$L_{\rm X}$ (10^{43} erg s^{-1})	Photon Index
AT2022abfc	20221208	17	<2	<6	2.49	<3	⋯
AT2023fhn	20230425	13	<1.7	<5	2.26	<4	⋯
AT2023hkw	20230521	21	<1.1	<3.5	1.05	<4.5	⋯
AT2023vth	20231110	21	<1.9	<3.4	22.6	<0.23	⋯
AT2024qfm	20240801	5	5.0 ± 0.8	13 ± 2	3.83	8.2 ± 1.3	$2.1^{+0.8}_{-0.5}$
AT2024qfm	20240802	6	3.7 ± 0.9	10 ± 2	⋯	6.1 ± 1.5	$1.5^{+1.6}_{-0.9}$
AT2024qfm	20240803	7	<4.9	<12	⋯	<7.9	⋯
AT2024qfm	20240803	7.5	$2.8^{+1.8}_{-1.3}$	7^{+5}_{-3}	⋯	$4.5^{+2.9}_{-2.1}$	$2.9^{+3.3}_{-2.9}$
AT2024qfm	20240805	9	<3.1	<8	⋯	<5.0	⋯
AT2024qfm	20240807	11	25^{+24}_{-14}	63^{+60}_{-35}	⋯	40^{+38}_{-23}	⋯[a]
AT2024qfm	20240809	13	<23	<58	⋯	<37	⋯
AT2024qfm	20240809	13.5	$2.0^{+1.2}_{-0.9}$	$5^{+3.2}_{-2.4}$	⋯	$3.3^{+2.0}_{-1.4}$	⋯[a]
AT2024qfm	20240810	14	$1.7^{+1.0}_{-0.7}$	$4^{+1.9}_{-2.7}$	⋯	$2.7^{+1.6}_{-1.2}$	$-0.3^{+1.5}_{-1.8}$
AT2024qfm	20240813	17	$2.6^{+1.5}_{-1.1}$	7^{+4}_{-3}	⋯	$4.2^{+2.5}_{-1.9}$	⋯[a]
AT2024qfm	20241204	130	<0.9	<2	⋯	<1.5	⋯
AT2024aehp	20241231	12	<2.3	<6.2	2.83	<2.0	⋯
AT2024aehp	20250103	15	<3.0	<7.9	⋯	<2.6	⋯
AT2024aehp	20250105	17	<2.4	<6.3	⋯	<2.1	⋯
CSS161010	20161103	24	$1.8^{+1.4}_{-0.9}$	$4.5^{+3.4}_{-2.3}$	4.7	$4.8^{+3.6}_{-2.4} \times 10^{-2}$	⋯[a]
CSS161010	20161108	29	<1.2	<2.9	⋯	$<3.4 \times 10^{-2}$	⋯
CSS161010	20161111	32	<2.0	<5.0	⋯	$<5.7 \times 10^{-2}$	⋯

Notes. AT2022abfc values are from A. Y. Q. Ho et al. (2022a), AT2023fhn measurements obtained from A. A. Chrimes et al. (2024b), and $n_{\rm H}$ for CSS161010 obtained from D. L. Coppejans et al. (2020). To convert flux to count rate, we assume a photon power-law index of $\Gamma = 2$ for all measurements. t is determined from the middle of the observation period. $n_{\rm H}$ is the same for all observations of a given object.
[a] Too few counts for a spectral index.

Table 4
Radio and Millimeter Observations

Name	UTC Date (YYYYMMDD)	t_{obs} (days)	Band	ν (GHz)	Config.	f_{ν} (μJy)
AT2022abfc	20221206	15	X	9	VLA-C	<17
AT2022abfc	20221206	15	X	11	VLA-C	<19
AT2022abfc	20221223	32	Ku	15	VLA-C	52 ± 3
AT2022abfc	20221223	32	X	10	VLA-C	38 ± 4
AT2022abfc	20230110	53	1	86	NOEMA-12A	<348
AT2022abfc	20230405	135	Ku	10	VLA-B	45 ± 7
AT2022abfc	20230405	135	X	10	VLA-B	43 ± 9
AT2022abfc	20230602	193	3	0.45	GMRT	<150
AT2022abfc	20230622	214	5	1.37	GMRT	44±12[a]
AT2022abfc	20230623	215	3	0.45	GMRT	<165
AT2022abfc	20230624	216	Ku	10	VLA-BnA− > A	<27
AT2022abfc	20230624	216	S	3	VLA-BnA− > A	<26
AT2022abfc	20230624	216	X	10	VLA-BnA− > A	<26
AT2022abfc	20240202	438	X	9	VLA-C	<17
AT2022abfc	20240202	438	X	11	VLA-C	<19
AT2023fhn	20230422	10	1	86	NOEMA-C	<90
AT2023fhn	20230511	29	X	9	VLA-B	<19
AT2023fhn	20230511	29	X	11	VLA-B	<20
AT2023fhn	20230615	64	X	9	VLA-BnA	43 ± 6
AT2023fhn	20230615	64	X	11	VLA-BnA	53 ± 7
AT2023fhn	20230709	88	Ku	15	VLA-A	75 ± 7
AT2023fhn	20230825	135	Ku	15	VLA-A	98 ± 9
AT2023fhn	20230825	135	X	10	VLA-A	143 ± 7
AT2023fhn	20230910	151	4	0.65	GMRT	<300
AT2023fhn	20230910	151	5	1.37	GMRT	<180
AT2023fhn	20231026	197	5	1.37	GMRT	85 ± 24
AT2023fhn	20231103	205	4	0.65	GMRT	<231
AT2023fhn	20231127	229	4	0.65	GMRT	<210
AT2023fhn	20231127	229	5	1.37	GMRT	112 ± 20
AT2023fhn	20240624	440	X	10	VLA-B	33 ± 5
AT2023hkw	20230614	44	X	9	VLA-BnA	79 ± 6
AT2023hkw	20230614	44	X	11	VLA-BnA	103 ± 7
AT2023hkw	20230704	64	Ka	33	VLA-A	124 ± 11
AT2023hkw	20230704	64	Ku	10	VLA-A	152 ± 7
AT2023hkw	20230826	117	C	6	VLA-A	74 ± 7
AT2023hkw	20230826	117	X	10	VLA-A	85 ± 8

Notes. The full set of radio and millimeter observations for each LFBOT is available online in a machine-readable table. These tables include comments for specific observations. Listed frequencies are in the observer frame. Some X-band observations are split into two subbands, one with a central frequency at 9 GHz and the other at 11 GHz. We require SNR > 3 for a detection. Otherwise, we list the 3σ upper limits for a nondetection.
[a] This measurement was binned together with a GMRT Band-5 observation on 2023 June 2.

(This table is available in its entirety in machine-readable form in the online article.)

Table 5
Host-galaxy Photometry

Object	GALEX		Legacy Survey/PS1				NEOWISE		
	Far-UV	Near-UV	*g*	*r*	*i*	*z*	*w*1	*w*2	*w*3
AT2022abfc	⋯	21.550±0.310	19.057±0.002	18.124±0.001	17.698±0.001	17.464±0.002	17.356±0.007	17.568±0.015	15.875±0.073
AT2023fhn	⋯	20.913±0.200	19.452±0.006	18.912±0.006	18.606±0.009	18.566±0.009	18.796±0.024	18.755±0.051	⋯
AT2023hkw	⋯	21.898±0.086	20.706±0.014	19.669±0.012	⋯	18.996±0.010	18.833±0.022	19.097±0.051	⋯
AT2023vth	⋯	21.601±0.274	19.430±0.019	18.774±0.012	18.370±0.008	18.179±0.014	19.809±0.192	20.170±0.380	⋯
AT2024qfm	⋯	⋯	20.530±0.007	19.706±0.006	⋯	19.135±0.007	19.156±0.028	19.218±0.067	⋯
AT2024aehp	22.158±0.181	21.902±0.115	20.881±0.009	20.454±0.009	20.240±0.013	20.232±0.020	20.761±0.117	20.468±0.206	⋯

Note. Photometry used in our `prospector` host-galaxy fits. Empty columns represent nondetections or detections with SNR < 5. The middle columns represent photometry in the Legacy Survey *griz* filters, or the PS1 *griz* filters for AT2023vth as its host was outside the Legacy Survey footprint. Not listed is HST photometry for AT2023fhn from A. A. Chrimes et al. (2024a) that was also used in the fit.

Table 6
Host-galaxy Properties

Object	Mass ($\log M/M_{\odot}$)	Metallicity ($\log Z/Z_{\odot}$)	Age (Gyr)	SFR ($M_{\odot}$ yr^{-1})	Host Extinction (τ)
AT2022abfc	$10.80^{+0.02}_{-0.04}$	0.05	$1.0^{+0.1}_{-0.2}$	$4.3^{+0.6}_{-0.6}$	$0.83^{+0.04}_{-0.04}$
AT2023fhn	$10.07^{+0.06}_{-0.06}$	−0.27	$0.7^{+0.5}_{-0.2}$	$7.7^{+1.4}_{-1.1}$	$0.59^{+0.05}_{-0.05}$
AT2023hkw	$10.7^{+0.1}_{-0.1}$	0.03	$2.7^{+1.2}_{-0.8}$	$2.8^{+1.3}_{-0.8}$	$0.22^{+0.17}_{-0.14}$
AT2023vth	$8.95^{+0.03}_{-0.04}$	−0.60	$0.62^{+0.13}_{-0.07}$	$0.24^{+0.04}_{-0.03}$	$0.0035^{+0.0055}_{-0.0026}$
AT2024qfm	$10.2^{+0.2}_{-0.1}$	−0.20	$4.4^{+5.0}_{-3.1}$	$3.3^{+1.1}_{-1.1}$	$0.60^{+0.14}_{-0.13}$
AT2024aehp	$8.9^{+0.1}_{-0.1}$	−0.60	$0.8^{+0.3}_{-0.3}$	$1.6^{+0.2}_{-0.2}$	$0.63^{+0.05}_{-0.05}$

Note. Results of our `prospector` host-galaxy fits. Metallicities were not determined by the fitting process, but by using a preliminary run at $\log Z/Z_{\odot} = -0.2$, and then converting the mass estimate to a metallicity using A. Gallazzi et al. (2005). For the host-galaxy extinction, we report the `dust2` parameter. FSPS defines this parameter as the optical depth τ in an extinction factor of $e^{-\tau}$ at the wavelength of 5500 Å.

Table 7
Radio Spectral Energy Distribution Broken Power-law Fit Parameters

Object	Observer-frame Epoch (days)	Rest-frame Epoch (days)	$\nu_{\rm obs}$ (GHz)	$F_{\rm obs}$ (μJy)	a_2
AT2023fhn	88–96	71–77	4.0 ± 0.3	232 ± 14	−0.69 ± 0.08
AT2023fhn	137–138	110–111	5.5 ± 0.3	387 ± 14	−0.87 ± 0.08
AT2023vth	86–87	80–81	8.5 ± 0.6	(2.6 ± 0.2) × 10^3	−1.06 ± 0.06
AT2023vth	104–129	97–120	2.7 ± 0.2	(1.50 ± 0.13) × 10^3	−0.55 ± 0.04
AT2024aehp	140–155	120–132	12.8 ± 1.1	(7.8 ± 0.9) × 10^2	−0.67 ± 0.09

Note. Results of a broken power-law fit (Equation 7). The values for the fitted peak frequency and flux density is measured in the observer's frame.

Table 8
Inferred Parameters from Synchrotron Self-absorption Modeling

Object	$t_{\rm rest}$ (days)	$\nu_{\rm p}$ (rest) (GHz)	R (10^{16} cm)	B (G)	v/c	Energy (10^{48} erg)	n_e (10^3 cm^{-3})	$\dot{M}$ (10^{-4} $M_{\odot}$ yr^{-1})	$m_p n_e R^3$ (10^{-5} $M_{\odot}$)
AT2022abfc	26	>19	<1.4	>1.49	<0.21	<1.7	>5.2	>0.35	>1.3
AT2023fhn	73	5.0 ± 0.4	13.0 ± 1.1	0.32 ± 0.03	0.57 ± 0.05	55 ± 6	0.022 ± 0.007	0.12 ± 0.02	4.1 ± 1.7
AT2023fhn	111	6.8 ± 0.4	12.0 ± 0.7	0.41 ± 0.02	0.38 ± 0.02	74 ± 5	0.10 ± 0.03	0.47 ± 0.06	15.2 ± 4.5
AT2023hkw	33	>15	<4.2	>0.95	<0.44	<16	>0.40	>0.22	>2.4
AT2023hkw	87	>8.0	<9.2	>0.5	<0.37	<47	>0.16	>0.43	>10.3
AT2023vth	81	9.1 ± 0.7	7.1 ± 0.6	0.58 ± 0.04	0.32 ± 0.03	31 ± 3	0.31 ± 0.09	0.49 ± 0.07	9.4 ± 3.6
AT2023vth	110	2.9 ± 0.2	17.6 ± 1.3	0.19 ± 0.01	0.53 ± 0.04	50 ± 6	0.010 ± 0.003	0.10 ± 0.01	4.7 ± 1.6
AT2024qfm	10	>115	<0.3	>8.32	<0.13	<0.58	>449	>1.48	>1.3
AT2024aehp	73	>18	<1.5	>1.36	<0.08	<1.7	>30	>2.22	>9.2
AT2024aehp	127	15.0 ± 1.3	5.5 ± 0.5	0.91 ± 0.08	0.16 ± 0.02	34 ± 5	3.1 ± 1.1	3.0 ± 0.5	44 ± 20

Note. The shock parameters we derive using Equations (2)–(6) for the various epochs of radio observations of each LFBOT. When we can only constrain the peak of the radio SED by observing one side of the broken power law, we calculate limits on these parameters using the observation closest to where the peak would be. The rightmost column is an estimate of the total mass swept up by the shock assuming a constant n_e.

Table 9
Optical Photometry

Object	UTC Time (YYYYMMDD HH:MM)	t_{rest} (days)	Facility	Filter	mag
AT2022abfc	20221114 08:31	−6	P48/ZTF	r	>19.68
AT2022abfc	20221114 10:40	−6	P48/ZTF	g	>19.65
AT2022abfc	20221115 09:09	−5	P48/ZTF	r	>20.40
AT2022abfc	20221115 10:08	−5	P48/ZTF	g	>20.19
AT2022abfc	20221116 08:19	−4	P48/ZTF	r	>19.36
AT2022abfc	20221117 08:01	−3	P48/ZTF	g	>19.69
AT2022abfc	20221117 08:48	−3	P48/ZTF	r	>19.53
AT2022abfc	20221118 08:04	−2	P48/ZTF	g	>20.51
AT2022abfc	20221118 09:32	−2	P48/ZTF	r	>20.13
AT2022abfc	20221119 09:34	−2	P48/ZTF	g	>19.71
AT2022abfc	20221120 08:01	−1	P48/ZTF	r	>20.35
AT2022abfc	20221121 08:15	0	P48/ZTF	r	19.46 ± 0.11
AT2022abfc	20221121 09:03	0	P48/ZTF	g	19.49 ± 0.14
AT2022abfc	20221125 08:32	3	P48/ZTF	r	19.55 ± 0.16
AT2022abfc	20221125 09:32	3	P48/ZTF	g	19.71 ± 0.20
AT2022abfc	20221127 07:32	5	P48/ZTF	r	20.32 ± 0.32
AT2022abfc	20221127 08:29	5	P48/ZTF	g	20.21 ± 0.19
AT2022abfc	20221201 09:15	8	P48/ZTF	r	>20.23
AT2022abfc	20221210 07:04	16	P48/ZTF	g	>19.60
AT2022abfc	20221211 07:03	16	P48/ZTF	g	>19.85
AT2022abfc	20221217 06:01	21	P48/ZTF	g	>20.35
AT2022abfc	20221217 07:03	21	P48/ZTF	r	>20.19
AT2022abfc	20221220 06:11	24	P48/ZTF	r	>19.21
AT2022abfc	20221220 07:03	24	P48/ZTF	g	>19.66
AT2023fhn	20230408 06:00	−3	P48/ZTF	i	>19.54
AT2023fhn	20230408 06:29	−3	P48/ZTF	g	>18.76
AT2023fhn	20230408 07:12	−3	P48/ZTF	r	>19.17
AT2023fhn	20230410 04:53	−2	P48/ZTF	r	19.68 ± 0.09
AT2023fhn	20230411 04:35	−1	P48/ZTF	i	19.65 ± 0.1
AT2023fhn	20230412 03:51	0	P48/ZTF	r	19.13 ± 0.05
AT2023fhn	20230412 04:35	0	P48/ZTF	g	18.69 ± 0.03
AT2023fhn	20230412 05:22	0	P48/ZTF	g	18.63 ± 0.03
AT2023fhn	20230412 05:27	0	P48/ZTF	g	18.72 ± 0.03
AT2023fhn	20230417 05:05	4	P48/ZTF	g	20.09 ± 0.09
AT2023fhn	20230417 05:49	4	P48/ZTF	r	20.72 ± 0.15
AT2023fhn	20230419 04:40	6	P60/SEDM	g	>19.30
AT2023fhn	20230419 04:44	6	P60/SEDM	r	>19.93
AT2023fhn	20230419 05:20	6	P48/ZTF	r	20.57 ± 0.22

Note. The full set of photometry for all six LFBOTs obtained from Fritz marshal are available online in a machine-readable table. We omit all observations prior to 6 days before t_0 and all ZTF nondetections more than 50 days after t_0. For nondetections, we provide 3σ upper limits.

(This table is available in its entirety in machine-readable form in the online article.)

ORCID iDs

Cassie Sevilla https://orcid.org/0009-0003-2780-704X
Anna Y. Q. Ho https://orcid.org/0000-0002-9017-3567
Nayana A.J. https://orcid.org/0000-0002-8070-5400
Steve Schulze https://orcid.org/0000-0001-6797-1889
Daniel A. Perley https://orcid.org/0000-0001-8472-1996
Igor Andreoni https://orcid.org/0000-0002-8977-1498
Thomas G. Brink https://orcid.org/0000-0001-5955-2502
Michael Camilo https://orcid.org/0000-0001-5593-0721
Poonam Chandra https://orcid.org/0000-0002-0844-6563
Ping Chen https://orcid.org/0000-0003-0853-6427
Ashley A. Chrimes https://orcid.org/0000-0001-9842-6808
Michael W. Coughlin https://orcid.org/0000-0002-8262-2924
Kaustav K. Das https://orcid.org/0000-0001-8372-997X
Andrew Drake https://orcid.org/0000-0003-0228-6594
Alexei V. Filippenko https://orcid.org/0000-0003-3460-0103
Christoffer Fremling https://orcid.org/0000-0002-4223-103X
James Freeburn https://orcid.org/0009-0006-7990-0547
Avishay Gal Yam https://orcid.org/0000-0002-3653-5598
Mary Gerhart https://orcid.org/0009-0009-5187-4123
Matthew J. Graham https://orcid.org/0000-0002-3168-0139
George Helou https://orcid.org/0000-0003-3367-3415
K-Ryan Hinds https://orcid.org/0000-0002-0129-806X
Natalya Johnson https://orcid.org/0009-0008-8062-445X
Mansi M. Kasliwal https://orcid.org/0000-0002-5619-4938
Harsh Kumar https://orcid.org/0000-0003-0871-4641
Russ R. Laher https://orcid.org/0000-0003-2451-5482
Natalie LeBaron https://orcid.org/0000-0002-2249-0595

Maggie L. Li https://orcid.org/0009-0001-6911-9144
Chang Liu https://orcid.org/0000-0002-7866-4531
Ben Margalit https://orcid.org/0000-0001-8405-2649
Yu-Jing Qin https://orcid.org/0000-0003-3658-6026
Nabeel Rehemtulla https://orcid.org/0000-0002-5683-2389
Sophia Risin https://orcid.org/0000-0002-1637-7668
Sam Rose https://orcid.org/0000-0003-4725-4481
Ben Rusholme https://orcid.org/0000-0001-7648-4142
Genevieve Schroeder https://orcid.org/0000-0001-9915-8147
Jesper Sollerman https://orcid.org/0000-0003-1546-6615
Gokul P. Srinivasaragavan https://orcid.org/0000-0002-6428-2700
Kailai Wang https://orcid.org/0009-0000-4756-4223
Jacob L. Wise https://orcid.org/0000-0003-0733-2916
Yi Yang https://orcid.org/0000-0002-6535-8500
Yuhan Yao https://orcid.org/0000-0001-6747-8509
WeiKang Zheng https://orcid.org/0000-0002-2636-6508

References

Andreoni, I., Coughlin, M. W., Kool, E. C., et al. 2021, ApJ, 918, 63
Bellm, E. C., Kulkarni, S. R., Graham, M. J., et al. 2019, PASP, 131, 018002
Berger, E., Kulkarni, S. R., Pooley, G., et al. 2003, Natur, 426, 154
Bhandari, S., Heintz, K. E., Aggarwal, K., et al. 2022, AJ, 163, 69
Bida, T. A., Dunham, E. W., Massey, P., & Roe, H. G. 2014, SPIE, 9147, 91472N
Bietenholz, M. F., Bartel, N., Argo, M., et al. 2021, ApJ, 908, 75
Blagorodnova, N., Gezari, S., Hung, T., et al. 2017, ApJ, 844, 46
Blagorodnova, N., Neill, J. D., Walters, R., et al. 2018, PASP, 130, 035003
Blanchard, P. K., Berger, E., & Fong, W.-f. 2016, ApJ, 817, 144
Blanchard, P. K., Nicholl, M., Berger, E., et al. 2017, ApJ, 843, 106
Briggs, D. S. 1995, PhD thesis, New Mexico Inst. of Mining and Technology
Bright, J. S., Margutti, R., Matthews, D., et al. 2022, ApJ, 926, 112
Burrows, D. N., Hill, J. E., Nousek, J. A., et al. 2005, SSRv, 120, 165
Calzetti, D., Armus, L., Bohlin, R. C., et al. 2000, ApJ, 533, 682
Campana, S., Mangano, V., Blustin, A. J., et al. 2006, Natur, 442, 1008
Cendes, Y., Berger, E., Alexander, K. D., et al. 2024, ApJ, 971, 185
Cenko, S. B., Fox, D. B., Moon, D.-S., et al. 2006, PASP, 118, 1396
Chabrier, G. 2003, PASP, 115, 763
Chambers, K. C., Magnier, E. A., Metcalfe, N., et al. 2016, arXiv:1612.05560
Chevalier, R. A. 1998, ApJ, 499, 810
Chevalier, R. A., & Fransson, C. 2006, ApJ, 651, 381
Chrimes, A., Jonker, P., Levan, A., Coppejans, D., & Malesani, D. B. 2023, TNSAN, 105, 1
Chrimes, A. A., Coppejans, D. L., Jonker, P. G., et al. 2024a, A&A, 691, A329
Chrimes, A. A., Jonker, P. G., Levan, A. J., & Mummery, A. 2026, A&A, 706, A327
Chrimes, A. A., Jonker, P. G., Levan, A. J., et al. 2024b, MNRAS, 527, L47
Clemens, J. C., Crain, J. A., & Anderson, R. 2004, SPIE, 5492, 331
Comrie, A., Wang, K.-S., Hsu, S.-C., et al. 2021, CARTA: The Cube Analysis and Rendering Tool for Astronomy, v2.0.0, Zenodo, doi:10.5281/zenodo.3377984
Coppejans, D. L., Margutti, R., Terreran, G., et al. 2020, ApJL, 895, L23
Corsi, A., Ofek, E. O., Gal-Yam, A., et al. 2014, ApJ, 782, 42
Coughlin, M. W., Bloom, J. S., Nir, G., et al. 2023, ApJS, 267, 31
De, K., Kasliwal, M. M., Tzanidakis, A., et al. 2020, ApJ, 905, 58
Dekany, R., Smith, R. M., Riddle, R., et al. 2020, PASP, 132, 038001
Dey, A., Schlegel, D. J., Lang, D., et al. 2019, AJ, 157, 168
Djupvik, A. A., & Andersen, J. 2010, ASSP, 14, 211
Dressler, A. 2011, PASP, 123, 288
Drout, M. R., Chornock, R., Soderberg, A. M., et al. 2014, ApJ, 794, 23
Duev, D. A., Mahabal, A., Masci, F. J., et al. 2019, MNRAS, 489, 3582
Evans, C. R., & Kochanek, C. S. 1989, ApJL, 346, L13
Faber, S.M., Phillips, A. C., Kibrick, R. I., et al. 2003, SPIE, 4841, 1657
Fabricant, D., Fata, R., Epps, H., et al. 2019, PASP, 131, 075004
Ferguson, R., & Margalit, B. 2026, ApJ, 1000, 16
Flewelling, H. A., Magnier, E. A., Chambers, K. C., et al. 2020, ApJS, 251, 7
Fong, W.-f., Nugent, A. E., Dong, Y., et al. 2022, ApJ, 940, 56
Forster, F., Bauer, F. E., Pignata, G., et al. 2024, TNSTR, 2624, 1
Fremling, C. 2022, TNSTR, 3387, 1
Fremling, C. 2023a, TNSTR, 775, 1
Fremling, C. 2023b, TNSTR, 981, 1
Fremling, C. 2023c, TNSTR, 2714, 1
Fremling, C., Miller, A. A., Sharma, Y., et al. 2020, ApJ, 895, 32
French, K. D., Wevers, T., Law-Smith, J., Graur, O., & Zabludoff, A. I. 2020, SSRv, 216, 32
Fulton, M., Chen, T. W., Smartt, S. J., et al. 2024, TNSAN, 206, 1
Gallazzi, A., Charlot, S., Brinchmann, J., White, S. D. M., & Tremonti, C. A. 2005, MNRAS, 362, 41
Gehrels, N., Chincarini, G., Giommi, P., et al. 2004, ApJ, 611, 1005
Gezari, S. 2021, ARA&A, 59, 21
Team, G. 2013, GILDAS: Grenoble Image and Line Data Analysis Software, Astrophysics Source Code Library, ascl:1305.010
Gillanders, J. H., Huber, M., Chambers, K., et al. 2024, TNSAN, 210, 1
Gimeno, G., Roth, K., Chiboucas, K., et al. 2016, SPIE, 9908, 99082S
Gottlieb, O., Tchekhovskoy, A., & Margutti, R. 2022, MNRAS, 513, 3810
Graham, M. J., Kulkarni, S. R., Bellm, E. C., et al. 2019, PASP, 131, 078001
Gutiérrez, C. P., Mattila, S., Lundqvist, P., et al. 2024, ApJ, 977, 162
Hinkle, J. T., Holoien, T. W.-S., Auchettl, K., et al. 2021, MNRAS, 500, 1673
Ho, A. Y. Q. 2023a, TNSAN, 174, 1
Ho, A. Y. Q. 2023b, TNSAN, 173, 1
Ho, A. Y. Q. 2023c, TNSAN, 317, 1
Ho, A. Y. Q. 2024, TNSAN, 211, 1
Ho, A. Y. Q., & Bremer, M. 2023, TNSAN, 318, 1
Ho, A. Y. Q., Liu, C., Andreoni, I., et al. 2023a, TNSAN, 93, 1
Ho, A. Y. Q., Liu, C., Chen, P., et al. 2022a, TNSAN, 275, 1
Ho, A. Y. Q., Phinney, E. S., Ravi, V., et al. 2019, ApJ, 871, 73
Ho, A. Y. Q., Perley, D. A., Kulkarni, S. R., et al. 2020a, ApJ, 895, 49
Ho, A. Y. Q., Perley, D. A., Beniamini, P., et al. 2020b, ApJ, 905, 98
Ho, A. Y. Q., Margalit, B., Bremer, M., et al. 2022b, ApJ, 932, 116
Ho, A. Y. Q., Perley, D. A., Yao, Y., et al. 2022c, ApJ, 938, 85
Ho, A. Y. Q., Perley, D. A., Gal-Yam, A., et al. 2023b, ApJ, 949, 120
Ho, A. Y. Q., Perley, D. A., Chen, P., et al. 2023c, Natur, 623, 927
Hook, I. M., Jørgensen, I., Allington-Smith, J. R., et al. 2004, PASP, 116, 425
Horesh, A., Cenko, S. B., & Arcavi, I. 2021, NatAs, 5, 491
Inkenhaag, A., Levan, A. J., Mummery, A., & Jonker, P. G. 2025, MNRAS, 544, L108
Inserra, C. 2019, NatAs, 3, 697
Ivezić, Ž., Kahn, S. M., Tyson, J. A., et al. 2019, ApJ, 873, 111
Johnson, B. D., Leja, J., Conroy, C., & Speagle, J. S. 2021, ApJS, 254, 22
Kansky, J., Chilingarian, I., Fabricant, D., et al. 2019, PASP, 131, 075005
Kelly, P. L., & Kirshner, R. P. 2012, ApJ, 759, 107
Kim, Y.-L., Rigault, M., Neill, J. D., et al. 2022, PASP, 134, 024505
Klencki, J., & Metzger, B. D. 2026, ApJ, 1005, 2
Kraft, R. P., Burrows, D. N., & Nousek, J. A. 1991, ApJ, 374, 344
Kremer, K., Lu, W., Piro, A. L., et al. 2021, ApJ, 911, 104
Kremer, K., Mockler, B., Piro, A. L., & Lombardi, J. C. 2023, MNRAS, 524, 6358
Kuin, N. P. M., Wu, K., Oates, S., et al. 2019, MNRAS, 487, 2505
Kulkarni, S. R., Frail, D. A., Wieringa, M. H., et al. 1998, Natur, 395, 663
Kulkarni, S. R., Harrison, F. A., Grefenstette, B. W., et al. 2021, arXiv:2111.15608
Labrie, K., Simpson, C., Cardenes, R., et al. 2023, RNAAS, 7, 214
Laskar, T., Alexander, K. D., & Berger, E. 2016, GCN, 20328, 1
Laskar, T., Berger, E., Chornock, R., et al. 2018, GCN, 23519, 1
Law-Smith, J., Ramirez-Ruiz, E., Ellison, S. L., & Foley, R. J. 2017, ApJ, 850, 22
LeBaron, N., Margutti, R., Chornock, R., et al. 2026, ApJL, 997, L10
Leja, J., Johnson, B. D., Conroy, C., van Dokkum, P. G., & Byler, N. 2017, ApJ, 837, 170
Li, M. L., Ho, A. Y. Q., Filippenko, A. V., et al. 2023, TNSAN, 114, 1
Lunnan, R., Chornock, R., Berger, E., et al. 2015, ApJ, 804, 90
Lyman, J. D., Levan, A. J., Tanvir, N. R., et al. 2017, MNRAS, 467, 1795
Mahabal, A., Rebbapragada, U., Walters, R., et al. 2019, PASP, 131, 038002
Mainzer, A., Bauer, J., Grav, T., et al. 2011, ApJ, 731, 53
Mandigo-Stoba, M. S., Fremling, C., & Kasliwal, M. 2022, JOSS, 7, 3612
Margalit, B., & Quataert, E. 2021, ApJL, 923, L14
Margalit, B., & Quataert, E. 2024, ApJ, 977, 134
Margutti, R., Nayana, A. J., & Sears, H. 2024, ATel, 16748, 1
Margutti, R., Metzger, B. D., Chornock, R., et al. 2019, ApJ, 872, 18
Martin, D. C., Fanson, J., Schiminovich, D., et al. 2005, ApJL, 619, L1
Masci, F. J., Laher, R. R., Rusholme, B., et al. 2019, PASP, 131, 018003
Matthews, D., Margutti, R., Metzger, B. D., et al. 2023, RNAAS, 7, 126
Merloni, A., Lamer, G., Liu, T., et al. 2024, A&A, 682, A34
Metzger, B. D. 2022, ApJ, 932, 84
Metzger, B. D., & Perley, D. A. 2023, ApJ, 944, 74
Million, C., Fleming, S. W., Shiao, B., et al. 2016, ApJ, 833, 292

Morrissey, P., Matuszewski, M., Martin, D. C., et al. 2018, ApJ, 864, 93
Munoz-Arancibia, A., Pignata, G., Bauer, F. E., et al. 2024, TNSTR, 4959, 1
Nayana, A. J., Margutti, R., Wiston, E., et al. 2025, ApJL, 993, L6
Nugent, A. E., Villar, V. A., Metzger, B. D., et al. 2026, ApJ, 1006, 75
Ofek, E. O., Rabinak, I., Neill, J. D., et al. 2010, ApJ, 724, 1396
Oke, J. B., & Gunn, J. E. 1982, PASP, 94, 586
Oke, J. B., & Gunn, J. E. 1983, ApJ, 266, 713
Oke, J. B., Cohen, J. G., Carr, M., et al. 1995, PASP, 107, 375
Patterson, M. T., Bellm, E. C., Rusholme, B., et al. 2019, PASP, 131, 018001
Perley, D. 2023, AAS Meeting, 241, 252.05
Perley, D. A. 2013, GCN, 14494, 1
Perley, D. A. 2019, PASP, 131, 084503
Perley, D. A., Schulze, S., & de Ugarte Postigo, A. 2017, GCN, 22252, 1
Perley, D. A., Mazzali, P. A., Yan, L., et al. 2019, MNRAS, 484, 1031
Perley, D. A., Ho, A. Y. Q., Yao, Y., et al. 2021, MNRAS, 508, 5138
Perley, D. A., Ho, A. Y. Q., McGrath, Z., et al. 2026, MNRAS, 549, stag678
Perley, R. A., Chandler, C. J., Butler, B. J., & Wrobel, J. M. 2011, ApJL, 739, L1
Pian, E., Amati, L., Antonelli, L. A., et al. 2000, ApJ, 536, 778
Pieterse, D. L. A., Levan, A. J., Ravasio, M. E., et al. 2026, MNRAS, 548, stag555
Planck Collaboration, Aghanim, N., Akrami, Y., et al. 2020, A&A, 641, A6
Predehl, P., Andritschke, R., Arefiev, V., et al. 2021, A&A, 647, A1
Prentice, S. J., Maguire, K., Smartt, S. J., et al. 2018, ApJL, 865, L3
Prochaska, J. X., Hennawi, J. F., Westfall, K. B., et al. 2020, JOSS, 5, 2308
Pursiainen, M., Childress, M., Smith, M., et al. 2018, MNRAS, 481, 894
Pursiainen, M., Killestein, T. L., Kuncarayakti, H., et al. 2025, MNRAS, 537, 3298
R Core Team 2025, R: A Language and Environment for Statistical Computing, R Foundation for Statistical Computing (The R Foundation), https://www.R-project.org/
Rigault, M., Neill, J. D., Blagorodnova, N., et al. 2019, A&A, 627, A115
Rivera Sandoval, L. E., Maccarone, T. J., Corsi, A., et al. 2018, MNRAS, 480, L146
Roming, P. W. A., Kennedy, T. E., Mason, K. O., et al. 2005, SSRv, 120, 95
Roux de Bezieux, H. 2024, Ecume: Equality of 2 (or k) Continuous Univariate and Multivariate Distributions,
Salas, P., Bauer, F. E., Stockdale, C., & Prieto, J. L. 2013, MNRAS, 428, 1207
Schlafly, E. F., & Finkbeiner, D. P. 2011, ApJ, 737, 103
Schroeder, G., Chen, P., Sollerman, J., et al. 2025, TNSAN, 3, 1
Schroeder, G., & Ho, A. Y. Q. 2025, TNSAN, 99, 1
Schulze, S., Yaron, O., Sollerman, J., et al. 2021, ApJS, 255, 29
Sevilla, J., Ho, A. Y. Q., & Srinivasaragavan, G. 2024, TNSAN, 386, 1
Sevilla, J., Li, M. L., & Ho, A. Y. Q. 2023, TNSAN, 297, 1
Shvartzvald, Y., Waxman, E., Gal-Yam, A., et al. 2024, ApJ, 964, 74
Silverman, J. M., Foley, R. J., Filippenko, A. V., et al. 2012, MNRAS, 425, 1789
Soderberg, A. M., Brunthaler, A., Nakar, E., Chevalier, R. A., & Bietenholz, M. F. 2010a, ApJ, 725, 922
Soderberg, A. M., Chevalier, R. A., Kulkarni, S. R., & Frail, D. A. 2006a, ApJ, 651, 1005
Soderberg, A. M., Kulkarni, S. R., Nakar, E., et al. 2006b, Natur, 442, 1014
Soderberg, A. M., Chakraborti, S., Pignata, G., et al. 2010b, Natur, 463, 513
Somalwar, J. J., Ravi, V., Margutti, R., et al. 2025, ApJ, 995, 228
Steele, I. A., Smith, R. J., Rees, P. C., et al. 2004, SPIE, 5489, 679
Sunyaev, R., Arefiev, V., Babyshkin, V., et al. 2021, A&A, 656, A132
Swarup, G., Ananthakrishnan, S., Kapahi, V. K., et al. 1991, CSci, 60, 95
Tachibana, Y., & Miller, A. A. 2018, PASP, 130, 128001
Taggart, K., & Perley, D. A. 2021, MNRAS, 503, 3931
Team, T. C., Bean, B., Bhatnagar, S., et al. 2022, PASP, 134, 114501
Thompson, A. R., Clark, B. G., Wade, C. M., & Napier, P. J. 1980, ApJS, 44, 151
Tiengo, A., Mereghetti, S., Ghisellini, G., Tavecchio, F., & Ghirlanda, G. 2004, A&A, 423, 861
Tody, D. 1986, SPIE, 627, 733
Tonry, J. L., Denneau, L., Heinze, A. N., et al. 2018, PASP, 130, 064505
Tsuna, D., & Lu, W. 2025, ApJ, 986, 84
Tsuna, D., Wu, S. C., Fuller, J., Dong, Y., & Piro, A. L. 2024, OJAp, 7, 82
Tubín-Arenas, D., Krumpe, M., Lamer, G., et al. 2024, A&A, 682, A35
van der Horst, A. J., Kamble, A., Resmi, L., et al. 2008, A&A, 480, 35
van der Walt, S., Crellin-Quick, A., & Bloom, J. 2019, JOSS, 4, 1247
Wang, X., Wang, L., Filippenko, A. V., Zhang, T., & Zhao, X. 2013, Sci, 340, 170
Yao, Y., Lu, W., Harrison, F., et al. 2024, ApJ, 965, 39
Yao, Y., Ho, A. Y. Q., Medvedev, P., et al. 2022, ApJ, 934, 104
Zackay, B., Ofek, E. O., & Gal-Yam, A. 2016, ApJ, 830, 27
Zauderer, B. A., Berger, E., Soderberg, A. M., et al. 2011, Natur, 476, 425